Computer Physics Communications 276 (2022) 108367

Contents lists available at ScienceDirect

Computer Physics Communications

www.elsevier.com/locate/cpc

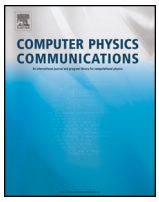

Axially-deformed solution of the Skyrme-Hartree-Fock-Bogoliubov equations using the transformed harmonic oscillator basis (IV) HFBTHO (v4.0): A new version of the program ☆,☆☆

P. Marević [a,b], N. Schunck [a,*], E.M. Ney [c], R. Navarro Pérez [d], M. Verriere [a], J. O'Neal [e]

[a] Nuclear and Chemical Science Division, Lawrence Livermore National Laboratory, Livermore, CA 94551, USA
[b] Department of Physics, Faculty of Science, University of Zagreb, HR-10000 Zagreb, Croatia
[c] Department of Physics and Astronomy, CB 3255, University of North Carolina, Chapel Hill, NC 27599-3255, USA
[d] Department of Physics, San Diego State University, 5500 Campanile Drive, San Diego, CA 02182-1233, USA
[e] Mathematics and Computer Science Division, Argonne National Laboratory, Lemont, IL 60439, USA

ARTICLE INFO

Article history:
Received 13 October 2021
Received in revised form 21 February 2022
Accepted 31 March 2022
Available online 11 April 2022

Keywords:
Energy density functional theory
Self-consistent mean field
Hartree-Fock-Bogoliubov theory
Harmonic oscillator
Restoration of symmetries
Angular momentum projection
Particle number projection
Distributed memory parallelism

ABSTRACT

We describe the new version 4.0 of the code HFBTHO that solves the nuclear Hartree-Fock-Bogoliubov problem by using the deformed harmonic oscillator basis in cylindrical coordinates. In the new version, we have implemented the restoration of rotational, particle number, and reflection symmetry for even-even nuclei. The restoration of rotational symmetry does not require using bases closed under rotation. Furthermore, we added the SeaLL1 functional and improved the calculation of the Coulomb potential. Finally, we refactored the code to facilitate maintenance and future developments.

New version program summary
Program title: HFBTHO v4.0
CPC Library link to program files: https://doi.org/10.17632/c5g2f92by3.2
Code Ocean capsule: https://codeocean.com/capsule/5389629
Licensing provisions: GPLv3
Programming language: Fortran 2003
Journal reference of previous version: R.N. Pérez, N. Schunck, R.-D. Lasseri, C. Zhang and J. Sarich, Comput. Phys. Commun. 220 (2017) 363
Does the new version supersede the previous version: Yes
Reasons for the new version: This version adds new capabilities to restore broken symmetries and determine corresponding quantum numbers of even-even nuclei
Summary of revisions:

1. Angular momentum projection for even-even nuclei in a deformed basis;
2. Particle number projection for even-even nuclei in the quasiparticle basis;
3. Implementation of the SeaLL1 functional;
4. Expansion of the Coulomb potential onto Gaussians;
5. MPI-parallelization of a single HFBTHO execution;
6. Code refactoring.

Nature of problem: HFBTHO is a physics computer code that is used to model the structure of the nucleus. It is an implementation of the energy density functional (EDF) approach to atomic nuclei, where the energy of the nucleus is obtained by integration over space of some phenomenological energy density, which is itself a functional of the neutron and proton intrinsic densities. In the present version of HFBTHO, the energy density is derived either from the zero-range Skyrme or the finite-range Gogny effective two-body interaction between nucleons. Nuclear superfluidity is treated at the Hartree-Fock-Bogoliubov (HFB) approximation. Constraints on the nuclear shape allow probing the potential energy surface of the

☆ The review of this paper was arranged by Prof. Z. Was.
☆☆ This paper and its associated computer program are available via the Computer Physics Communications homepage on ScienceDirect (http://www.sciencedirect.com/science/journal/00104655).

* Corresponding author.
E-mail address: schunck1@llnl.gov (N. Schunck).

https://doi.org/10.1016/j.cpc.2022.108367

nucleus as needed, e.g., for the description of shape isomers or fission. A local scale transformation of the single-particle basis in which the HFB solutions are expanded provides a tool to properly compute the structure of weakly-bound nuclei. Restoration of the rotational, particle number, and reflection symmetry for even-even nuclei enables recovering the quantum numbers that are lost at the HFB approximation.
Solution method: The program uses the axial harmonic oscillator (HO) or the transformed harmonic oscillator (THO) single-particle basis to expand quasiparticle wave functions. It iteratively diagonalizes the HFB Hamiltonian based on generalized Skyrme-like energy densities and zero-range pairing interactions or the finite-range Gogny force until a self-consistent solution is found. Lagrange parameters are used to impose constraints on HFB solutions, and their value is updated at each iteration from an approximation of the quasiparticle random phase approximation (QRPA) matrix. Symmetry restoration is implemented through standard projection techniques. Previous versions of the program were presented in [1-3].
Additional comments including restrictions and unusual features: Axial and time-reversal symmetries are assumed in HFB calculations; y-simplex symmetry and even particle numbers are assumed in angular momentum projection.

References

[1] M. V. Stoitsov, J. Dobaczewski, W. Nazarewicz, P. Ring, Axially deformed solution of the Skyrme-Hartree-Fock-Bogolyubov equations using the transformed harmonic oscillator basis. The program HFBTHO (v1.66p), Comput. Phys. Commun. 167 (1) (2005) 43.
[2] M. Stoitsov, N. Schunck, M. Kortelainen, N. Michel, H. Nam, E. Olsen, J. Sarich, S. Wild, Axially deformed solution of the Skyrme-Hartree-Fock-Bogolyubov equations using the transformed harmonic oscillator basis (II) HFBTHO v2.00d: A new version of the program, Comput. Phys. Commun. 184 (6) (2013) 1592.
[3] R. N. Perez, N. Schunck, R.-D. Lasseri, C. Zhang, J. Sarich, Axially deformed solution of the Skyrme–Hartree–Fock–Bogolyubov equations using the transformed harmonic oscillator basis (III) HFBTHO (v3.00): A new version of the program, Comput. Phys. Commun. 220 (2017) 363.

1. Introduction

Over the past decades, the nuclear energy density functional (EDF) framework has become a tool of choice for describing the properties of nuclear structure and reactions across the entire nuclide chart [1–4]. It closely resembles density functional theory (DFT), a method widely used in condensed matter physics and quantum chemistry, insofar that it employs the mean-field approximation to map a complex many-body problem onto a computationally feasible one-body problem. In nuclear physics, the EDF framework is typically realized at two distinct levels. The single-reference energy density functional (SR-EDF) method introduces relatively simple functionals of nucleon densities and currents, describing the nuclear ground states in terms of symmetry-breaking mean-field wave functions. Most of the EDF-based computer programs available on the market correspond to different flavors of the SR-EDF method; see, e.g., [5–10] for some selected examples. However, a more advanced description requires the inclusion of collective correlations related to the restoration of broken symmetries and quantum shape fluctuations. This is the basic tenet of the multi-reference energy density functional (MR-EDF) method.

The previous versions of the HFBTHO program are largely implementations of the SR-EDF formalism in the axial harmonic oscillator (HO) basis or the transformed harmonic oscillator (THO) basis [11,12,5]. The core of the program is a solver for the self-consistent Hartree-Fock-Bogoliubov (HFB) equation. While the initial release [11] was restricted to even-even nuclei with Skyrme EDFs and contact pairing interactions, more recent versions expanded the theoretical framework significantly: to describe parity-breaking shapes, nuclei with odd number of particles, and nuclei at finite temperature [12]; to solve the HFB equation for the finite-range Gogny potentials, compute the collective mass tensor and zero-point energy corrections, regularize the pairing interaction, and compute properties of fission fragments [5].

Among the publicly available codes, MR-EDF capabilities include the restoration of particle number symmetry in the canonical basis in HFBTHO (all versions) and the restoration of rotational, isospin, particle-number, and reflection symmetries of HFB states in HFODD 3.06h [13]. Note that HFODD projects either on total particle number A or total isospin projection T_z but not separately on the number of protons Z and neutrons N. Compared to previous versions of HFBTHO, the present release contains a much more expanded MR-EDF toolkit for symmetry restoration that is tailored for large-scale applications of the MR-EDF framework. Specifically, the version 4.0 of HFBTHO implements the restoration of rotational, particle number, and reflection symmetry for even-even nuclei. These restorations can be performed either independently (e.g., either the rotational and reflection symmetries only or the particle number symmetry only), or they can be combined in the joint restoration of all three types of quantum numbers (angular momentum, particle number, and parity). In addition, our implementation of the angular momentum restoration bypasses the need to use rotationally-invariant, closed bases. Symmetry restoration can now be performed in the deformed (stretched) HO basis typically employed in large-scale calculations of potential energy surfaces.

In Section 2, we review the modifications introduced in this version of the program. In Section 3, we give several numerical benchmarks for the new capabilities. Finally, in Section 4, we discuss the new options available in the input file and explain how to run the code.

2. Modifications introduced in version 4.0

In this section, we present the new features added to the code between version 3.00 and 4.0.

2.1. Restoration of broken symmetries

A module for restoration of broken symmetries is the main new feature of version 4.0. In the following, we describe the underlying theoretical framework in detail.

2.1.1. General framework

The HFB states break several symmetries of the nuclear Hamiltonian and consequently do not carry the associated good quantum numbers. Since its first published version, the HFBTHO program has

implemented the particle number restoration in the canonical basis for even-even nuclei. The current version includes a new module for the simultaneous restoration of rotational, particle number, and reflection symmetry of the HFB states for even-even nuclei [1,14,15].

The main ingredient of symmetry-restoring calculations are kernels of the form

$$O^{JMK;NZ;p}_{\boldsymbol{qq}} = \langle \Phi_{\boldsymbol{q}} | \hat{O}\, \hat{P}^J_{MK}\, \hat{P}^N\, \hat{P}^Z\, \hat{P}^p | \Phi_{\boldsymbol{q}} \rangle \,. \tag{1}$$

Here, $|\Phi_{\boldsymbol{q}}\rangle$ is an HFB state at point $\boldsymbol{q}$ in the collective space defined by the set of active constraints on the HFB solution, while $\hat{O}$ is either the identity operator for the norm overlap kernel, $O^{JMK;NZ;p}_{\boldsymbol{qq}} \equiv \mathcal{N}^{JMK;NZ;p}_{\boldsymbol{qq}}$, or the Hamiltonian operator for the Hamiltonian kernel, $O^{JMK;NZ;p}_{\boldsymbol{qq}} \equiv \mathcal{H}^{JMK;NZ;p}_{\boldsymbol{qq}}$.

The operator that projects an HFB state onto a state with good values of angular momentum J reads

$$\hat{P}^J_{MK} = \frac{2J+1}{16\pi^2} \int d\Omega\, D^{J*}_{MK}(\alpha,\beta,\gamma)\, \hat{R}(\alpha,\beta,\gamma), \tag{2}$$

where α, β, and γ are the usual Euler angles, $\int d\Omega \equiv \int_0^{2\pi} d\alpha \times \int_0^{\pi} d\beta \sin\beta \int_0^{4\pi} d\gamma$, and $D^J_{MK}(\alpha,\beta,\gamma)$ is the Wigner D-matrix [16]. The coordinate-space rotation operator reads

$$\hat{R}(\alpha,\beta,\gamma) = e^{-i\alpha \hat{J}_z} e^{-i\beta \hat{J}_y} e^{-i\gamma \hat{J}_z}. \tag{3}$$

Note that the conservation of number parity [17] allows reducing the integration interval over γ to $[0, 2\pi]$. This has no practical consequence in HFBTHO since integrals over Euler angles α and γ are trivial and can be carried out analytically due to the axial symmetry. In addition, the current version of HFBTHO computes kernels (1) for the identity and the Hamiltonian operator only. For such scalar operators, only the $M = K = 0$ components of the total angular momentum do not vanish identically.

Furthermore, the operator that projects an HFB state onto a state with a good number of particles reads

$$\hat{P}^X = \frac{1}{2\pi} \int_0^{2\pi} d\varphi\, e^{i(\hat{X} - X_0)\varphi}, \tag{4}$$

where $X = N\,(Z)$ is a label referring to neutrons (protons), $X_0 = N_0\,(Z_0)$ is the desired number of neutrons (protons), and $\hat{X} = \hat{N}\,(\hat{Z})$ is the neutron (proton) number operator. In practice, the integration interval over the gauge angle φ can be reduced to $[0, \pi]$ using the property of a good number parity of an HFB state. The resulting integral is further discretized and particle number projection is performed using the Fomenko expansion [18]

$$\hat{P}^X = \frac{1}{N_\varphi} \sum_{l_\tau=1}^{N_\varphi} e^{i(\hat{X} - X_0)\varphi_{l_\tau}}, \quad \varphi_{l_\tau} = \frac{\pi}{N_\varphi} l_\tau, \tag{5}$$

where $\tau = n\,(p)$ for neutrons (protons) and N_φ is the corresponding number of gauge angle points which may in principle be different for neutrons and protons.

Finally, the operator that projects an HFB state onto a state with good parity reads

$$\hat{P}^p = \frac{1}{2}\Big(1 + p\hat{\Pi}\Big), \tag{6}$$

where $p = +1\,(-1)$ for positive (negative) parity and $\hat{\Pi}$ is the standard parity operator [19].

Combining the expressions for projection operators and assuming the same number of gauge angle points for neutrons and protons, the kernels (1) can be written as

$$\begin{aligned} O^{J;NZ;p}_{\boldsymbol{qq}} = {} & \frac{2J+1}{2} \int_0^{\pi} d\beta\, \sin\beta\, d^{J*}_{00}(\beta) \\ & \times \frac{1}{N_\varphi^2} \sum_{l_n=1}^{N_\varphi} \sum_{l_p=1}^{N_\varphi} e^{-iN_0\varphi_{l_n}} e^{-iZ_0\varphi_{l_p}} \\ & \times \frac{1}{2}\Big[O_{\boldsymbol{qq}}(\beta,\varphi_{l_n},\varphi_{l_p}) + pO^{\pi}_{\boldsymbol{qq}}(\beta,\varphi_{l_n},\varphi_{l_p}) \Big], \end{aligned} \tag{7}$$

with the rotated kernels

$$O_{\boldsymbol{qq}}(\beta,\varphi_{l_n},\varphi_{l_p}) \equiv \langle \Phi_{\boldsymbol{q}} | \hat{O} e^{-i\beta \hat{J}_y} e^{i\varphi_{l_n}\hat{N}} e^{i\varphi_{l_p}\hat{Z}} | \Phi_{\boldsymbol{q}} \rangle \,, \tag{8a}$$

$$O^{\Pi}_{\boldsymbol{qq}}(\beta,\varphi_{l_n},\varphi_{l_p}) \equiv \langle \Phi_{\boldsymbol{q}} | \hat{O} e^{-i\beta \hat{J}_y} e^{i\varphi_{l_n}\hat{N}} e^{i\varphi_{l_p}\hat{Z}} \hat{\Pi} | \Phi_{\boldsymbol{q}} \rangle \,. \tag{8b}$$

The expression for kernels can be further simplified by using the symmetries of an HFB state. In particular, the anti-linear y-time-simplex operator $\hat{S}^T_y = \hat{\Pi}\hat{T} e^{-i\pi \hat{J}_y}$ fixes a phase through a symmetry transformation [20,21,15]

$$\hat{S}^T_y\, |\Phi_{\boldsymbol{q}}\rangle = |\Phi_{\boldsymbol{q}}\rangle \,. \tag{9}$$

Using the time-reversal symmetry, we then obtain the following relation for the rotated kernels

$$O^{\Pi}_{\boldsymbol{qq}}(\beta,\varphi_{l_n},\varphi_{l_p}) = O_{\boldsymbol{qq}}(\pi - \beta,\varphi_{l_n},\varphi_{l_p}). \tag{10}$$

This greatly facilitates calculations because only the rotated kernels $O_{\boldsymbol{qq}}(\beta,\varphi_{l_n},\varphi_{l_p})$ need to be evaluated explicitly. Moreover, since only diagonal kernels are considered in this version of the code, the second subscript $\boldsymbol{q}$ can be dropped. Therefore, the rotated kernels will simply be denoted as $O_{\boldsymbol{q}}(\beta,\varphi_{l_n},\varphi_{l_p})$.

The symmetry-restoring framework enables us to expand an HFB state $|\Phi_{\boldsymbol{q}}\rangle$ into a basis of states with good quantum numbers (angular momentum, particle number, parity) and to extract their respective coefficients [17]. For example, in the case of the particle number decomposition, we can write

$$|\Phi_{\boldsymbol{q}}\rangle = \sum_N \sum_Z c^{NZ}_{\boldsymbol{q}}\, |NZ\rangle \,, \tag{11}$$

and the coefficients satisfy

$$\big|c^{NZ}_{\boldsymbol{q}}\big|^2 = \frac{1}{N_\varphi^2} \sum_{l_n=1}^{N_\varphi} \sum_{l_p=1}^{N_\varphi} e^{-iN_0\varphi_{l_n}} e^{-iZ_0\varphi_{l_p}} O_{\boldsymbol{q}}(0,\varphi_{l_n},\varphi_{l_p}), \tag{12}$$

with $\sum_N \sum_Z |c^{NZ}_{\boldsymbol{q}}|^2 = 1$. Similarly, a decomposition onto states with good angular momenta and parity implies that the coefficients satisfy

$$\begin{aligned} \big|c^{J;p}_{\boldsymbol{q}}\big|^2 = {} & \frac{2J+1}{2} \int_0^{\pi} d\beta\, \sin\beta\, d^{J*}_{00}(\beta) \\ & \times \frac{1}{2}\Big[O_{\boldsymbol{q}}(\beta,0,0) + pO_{\boldsymbol{q}}(\pi-\beta,0,0) \Big], \end{aligned} \tag{13}$$

with $\sum_J \sum_p |c^{J;p}_{\boldsymbol{q}}|^2 = 1$. Note that only collective states obeying the natural spin-parity selection rule, $p = (-1)^J$, are accessible within the present model. The coefficients of the simultaneous expansion onto states with good angular momentum, particle number, and parity are given by Eq. (7), i.e., $|c^{J;NZ;p}_{\boldsymbol{q}}|^2 = O^{J;NZ;p}_{\boldsymbol{qq}}$. They satisfy the sum rule $\sum_J \sum_p \sum_{N,Z} |c^{J;NZ;p}_{\boldsymbol{q}}|^2 = 1$. Finally, the energy of a symmetry-restored state is calculated as

$$E^{J;NZ;p}_{\boldsymbol{q}} = \frac{\mathcal{H}^{J;NZ;p}_{\boldsymbol{q}}}{\mathcal{N}^{J;NZ;p}_{\boldsymbol{q}}}. \tag{14}$$

2.1.2. Bases not closed under rotation

Numerous implementations of the symmetry-restoring framework (see Refs. [3,4,22] and references therein for some recent results) relied on the expansion of HFB states in spherical HO bases that are closed under rotation. However, such an approach becomes computationally intractable when describing extremely heavy or deformed configurations like those appearing in studies of nuclear fission or the structure of superheavy nuclei. In these cases, numerical convergence can typically be achieved only by expanding HFB states in deformed HO bases with incomplete oscillator shells. However, such bases are not closed under rotation and the conventional symmetry-restoring framework is consequently inapplicable.[1]

The elegant solution to this hurdle was proposed almost three decades ago by L. Robledo [26], who reformulated Wick's theorem [27,28] to encompass bases not closed under rotation. The first implementations of the modified symmetry-restoring framework were reported only very recently [29,30]. Version 4.0 of HFBTHO is the first one to contain this capability. In particular, for the case of bases not closed under rotation, the rotated norm overlap kernel for particle type $\tau = n, p$ reads

$$\mathcal{N}_{\boldsymbol{q}}^{(\tau)}(\boldsymbol{x}^{(\tau)}) = \sqrt{\det\left[A_{\boldsymbol{q}}^{(\tau)}(\boldsymbol{x}^{(\tau)})\right]\det\left[R(\boldsymbol{x}^{(\tau)})\right]}, \tag{15}$$

where $\boldsymbol{x}^{(\tau)} \equiv \{\beta, \varphi_{l_\tau}\}$, $R(\boldsymbol{x}^{(\tau)})$ is the total rotation matrix, and the $A_{\boldsymbol{q}}^{(\tau)}(\boldsymbol{x}^{(\tau)})$ matrix reads

$$A_{\boldsymbol{q}}^{(\tau)}(\boldsymbol{x}^{(\tau)}) = U_{\boldsymbol{q}}^{(\tau)T}\left[R^T(\boldsymbol{x}^{(\tau)})\right]^{-1}U_{\boldsymbol{q}}^{(\tau)*} + V_{\boldsymbol{q}}^{(\tau)T}R(\boldsymbol{x}^{(\tau)})V_{\boldsymbol{q}}^{(\tau)*}. \tag{16}$$

Here, the Bogoliubov matrices $U_{\boldsymbol{q}}^{(\tau)}$, $V_{\boldsymbol{q}}^{(\tau)}$ correspond to the HFB solution $|\Phi_{\boldsymbol{q}}\rangle$ for particle τ. Without breaking the isospin symmetry, the full rotated norm overlap kernel is separable in isospin

$$\mathcal{N}_{\boldsymbol{q}}(\beta, \varphi_{l_n}, \varphi_{l_p}) = \mathcal{N}_{\boldsymbol{q}}^{(\tau=n)}(\beta, \varphi_{l_n}) \times \mathcal{N}_{\boldsymbol{q}}^{(\tau=p)}(\beta, \varphi_{l_p}). \tag{17}$$

Moreover, in the case of a basis closed under rotation we have $|\det[R(\boldsymbol{x}^{(\tau)})]| = 1$, and the expression (15) reduces to the conventional Onishi formula [31].

Furthermore, the rotated density and pairing tensors for particle type τ read

$$\rho_{\boldsymbol{q}}^{(\tau)}(\boldsymbol{x}^{\tau}) = R(\boldsymbol{x}^{(\tau)})V_{\boldsymbol{q}}^{(\tau)*}\left[A_{\boldsymbol{q}}^{(\tau)}(\boldsymbol{x}^{(\tau)})\right]^{-1}V_{\boldsymbol{q}}^{(\tau)T}, \tag{18a}$$

$$\kappa_{\boldsymbol{q}}^{(\tau)}(\boldsymbol{x}^{(\tau)}) = R(\boldsymbol{x}^{(\tau)})V_{\boldsymbol{q}}^{(\tau)*}\left[A_{\boldsymbol{q}}^{(\tau)}(\boldsymbol{x}^{(\tau)})\right]^{-1}U_{\boldsymbol{q}}^{(\tau)T}, \tag{18b}$$

$$\kappa_{\boldsymbol{q}}^{*(\tau)}(\boldsymbol{x}^{(\tau)}) = -R^*(\boldsymbol{x}^{(\tau)})U_{\boldsymbol{q}}^{(\tau)*}\left[A_{\boldsymbol{q}}^{(\tau)}(\boldsymbol{x}^{(\tau)})\right]^{-1}V_{\boldsymbol{q}}^{(\tau)T}. \tag{18c}$$

The rotated Hamiltonian kernel $\mathcal{H}_{\boldsymbol{q}}(\beta, \varphi_{l_n}, \varphi_{l_p})$ is a functional of the rotated density and pairing tensors; see Section 2.1.6 and Refs. [1,2] for more details.

2.1.3. Structure of matrices in the y-simplex basis

The rotation by an angle β about the y-axis of the reference frame breaks the axial symmetry of HFB solutions. Computations can thus be facilitated by using a non-axially-symmetric, computationally-efficient representation of the Bogoliubov matrices $U_{\boldsymbol{q}}^{(\tau)}$ and $V_{\boldsymbol{q}}^{(\tau)}$. This is achieved by introducing the y-simplex basis.

[1] Alternatively, symmetry restoration can also be performed with HFB states obtained in a coordinate-space representation [2]. To avoid the large computational cost associated to spatial rotations of HFB states during the angular momentum projection, the relevant kernels are often computed in the canonical basis. This can lead to similar difficulties as using incomplete HO bases; see [23–25] for a discussion.

The y-simplex basis. The HO basis states $|\alpha\rangle$ are characterized by the set of quantum numbers $\{\alpha\} = \{n_z^\alpha, n_\perp^\alpha, \Lambda^\alpha, \Sigma^\alpha\}$, where n_z^α and $n_\perp^\alpha$ represent the number of quanta (nodes) in the $z-$ and the $r_\perp-$ direction, respectively, while Λ^α and $\Sigma^\alpha(\equiv|\uparrow\rangle, |\downarrow\rangle)$ denote the components of the orbital angular momentum and of the spin along the z-axis. Starting from these initial basis states, it is straightforward to show that the linear combinations

$$\begin{aligned}
|n_z^\alpha n_\perp^\alpha \Lambda^\alpha; +\rangle &= \frac{1}{\sqrt{2}}\Big[\, i\,|n_z^\alpha n_\perp^\alpha \Lambda^\alpha \uparrow\rangle + |n_z^\alpha n_\perp^\alpha -\Lambda^\alpha \downarrow\rangle\,\Big], \\
|n_z^\alpha n_\perp^\alpha \Lambda^\alpha; -\rangle &= \frac{1}{\sqrt{2}}\Big[\, |n_z^\alpha n_\perp^\alpha \Lambda^\alpha \uparrow\rangle + i\,|n_z^\alpha n_\perp^\alpha -\Lambda^\alpha \downarrow\rangle\,\Big],
\end{aligned} \tag{19}$$

are eigenstates of the y-simplex operator $\hat{R}_y$ with eigenvalues of $+i$ and $-i$, respectively. The y-simplex operator $\hat{R}_y$ is defined as a rotation around the y-axis by an angle π, followed by the parity transformation $\hat{\Pi}$

$$\hat{R}_y = \hat{\Pi}\exp(-i\pi\,\hat{J}_y). \tag{20}$$

The y-simplex basis can be used to reduce the computational cost by exploiting symmetries of the problem at hand.

Bogoliubov matrices. In the y-simplex basis, the Bogoliubov matrices acquire the block structure

$$U_{\boldsymbol{q}}^{(\tau)} = \begin{pmatrix} u_{\boldsymbol{q}}^{(\tau)} & 0 \\ 0 & u_{\boldsymbol{q}}^{(\tau)*} \end{pmatrix}, \qquad V_{\boldsymbol{q}}^{(\tau)} = \begin{pmatrix} 0 & -v_{\boldsymbol{q}}^{(\tau)*} \\ v_{\boldsymbol{q}}^{(\tau)} & 0 \end{pmatrix}. \tag{21}$$

In this expression, the basis states are organized in two blocks: the first block comprises all states with an eigenvalue $+i$, while the second block comprises all states with an eigenvalue $-i$. The transformation between the components k of Bogoliubov matrices in the y-simplex basis and the HO basis reads

$$u_{\boldsymbol{q},k}^{(\tau)[n_z^\alpha, n_\perp^\alpha, \Omega^\alpha - \frac{1}{2}]} = (+1)U_{\boldsymbol{q},k}^{(\tau)[n_z^\alpha, n_\perp^\alpha, \Omega^\alpha - \frac{1}{2}, \Sigma^\alpha = +\frac{1}{2}]}, \tag{22a}$$

$$u_{\boldsymbol{q},k}^{(\tau)[n_z^\alpha, n_\perp^\alpha, -\Omega^\alpha - \frac{1}{2}]} = (+i)U_{\boldsymbol{q},k}^{(\tau)[n_z^\alpha, n_\perp^\alpha, \Omega^\alpha + \frac{1}{2}, \Sigma^\alpha = -\frac{1}{2}]}, \tag{22b}$$

$$v_{\boldsymbol{q},k}^{(\tau)[n_z^\alpha, n_\perp^\alpha, \Omega^\alpha - \frac{1}{2}]} = (-1)V_{\boldsymbol{q},k}^{(\tau)[n_z^\alpha, n_\perp^\alpha, \Omega^\alpha - \frac{1}{2}, \Sigma^\alpha = +\frac{1}{2}]}, \tag{22c}$$

$$v_{\boldsymbol{q},k}^{(\tau)[n_z^\alpha, n_\perp^\alpha, -\Omega^\alpha - \frac{1}{2}]} = (-i)V_{\boldsymbol{q},k}^{(\tau)[n_z^\alpha, n_\perp^\alpha, \Omega^\alpha + \frac{1}{2}, \Sigma^\alpha = -\frac{1}{2}]}. \tag{22d}$$

Using these expressions, one can construct $U_{\boldsymbol{q}}^{(\tau)}$ and $V_{\boldsymbol{q}}^{(\tau)}$ matrices in the y-simplex basis from the HFB solutions expressed in the HO basis.

Rotation matrix. The total rotation operator corresponds to the combination of a spatial rotation for an angle β and a gauge space rotation for an angle φ_{l_τ}. In the y-simplex basis, the rotation matrix acquires the following block structure

$$R(\boldsymbol{x}^{(\tau)}) = e^{i\varphi_{l_\tau}}\begin{pmatrix} r(\beta) & 0 \\ 0 & r^*(\beta) \end{pmatrix}, \tag{23}$$

where the matrix elements $r_{\alpha\gamma}(\beta)$ of the $r(\beta)$ matrix read

$$\begin{aligned}
r_{\alpha\gamma}(\beta) = &\frac{1}{2}\cos\left(\frac{\beta}{2}\right)\langle n_z^\alpha n_\perp^\alpha \Lambda^\alpha | e^{-i\beta\hat{L}_y} | n_z^\gamma n_\perp^\gamma \Lambda^\gamma\rangle \\
&+ \frac{1}{2}\cos\left(\frac{\beta}{2}\right)\langle n_z^\alpha n_\perp^\alpha -\Lambda^\alpha | e^{-i\beta\hat{L}_y} | n_z^\gamma n_\perp^\gamma -\Lambda^\gamma\rangle \\
&+ \frac{i}{2}\sin\left(\frac{\beta}{2}\right)\langle n_z^\alpha n_\perp^\alpha \Lambda^\alpha | e^{-i\beta\hat{L}_y} | n_z^\gamma n_\perp^\gamma -\Lambda^\gamma\rangle \\
&+ \frac{i}{2}\sin\left(\frac{\beta}{2}\right)\langle n_z^\alpha n_\perp^\alpha -\Lambda^\alpha | e^{-i\beta\hat{L}_y} | n_z^\gamma n_\perp^\gamma \Lambda^\gamma\rangle\,.
\end{aligned} \tag{24}$$

Matrix elements of the $e^{-i\beta\hat{L}_y}$ operator are evaluated using the prescription of Ref. [32].

Calculation of overlaps. Using the block structure of the Bogoliubov matrices and of the total rotation matrix, we can recast the $A_{\boldsymbol{q}}^{(\tau)}(\boldsymbol{x}^{(\tau)})$ matrix in the y-simplex basis as

$$A_{\boldsymbol{q}}^{(\tau)}(\boldsymbol{x}^{(\tau)}) = \begin{pmatrix} a_{\boldsymbol{q}}^{(\tau)++}(\boldsymbol{x}^{(\tau)}) & 0 \\ 0 & a_{\boldsymbol{q}}^{(\tau)--}(\boldsymbol{x}^{(\tau)}) \end{pmatrix}, \tag{25}$$

where

$$a_{\boldsymbol{q}}^{(\tau)++}(\boldsymbol{x}^{(\tau)}) = e^{-i\varphi_{l_\tau}} a_{U_{\boldsymbol{q}}}^{(\tau)}(\beta) + e^{i\varphi_{l_\tau}} a_{V_{\boldsymbol{q}}}^{(\tau)}(\beta), \tag{26a}$$

$$a_{\boldsymbol{q}}^{(\tau)--}(\boldsymbol{x}^{(\tau)}) = e^{-i\varphi_{l_\tau}} \left[a_{U_{\boldsymbol{q}}}^{(\tau)}(\beta)\right]^* + e^{i\varphi_{l_\tau}} \left[a_{V_{\boldsymbol{q}}}^{(\tau)}(\beta)\right]^*, \tag{26b}$$

and

$$a_{U_{\boldsymbol{q}}}^{(\tau)}(\beta) = \left[u_{\boldsymbol{q}}^{(\tau)}\right]^T \left[r^T(\beta)\right]^{-1} u_{\boldsymbol{q}}^{(\tau)*}, \tag{27a}$$

$$a_{V_{\boldsymbol{q}}}^{(\tau)}(\beta) = \left[v_{\boldsymbol{q}}^{(\tau)}\right]^T r^*(\beta) v_{\boldsymbol{q}}^{(\tau)*}. \tag{27b}$$

The rotated norm overlap kernel then reads

$$\mathcal{N}_{\boldsymbol{q}}^{(\tau)}(\boldsymbol{x}^{(\tau)}) = \sqrt{\det\left[\begin{pmatrix} n_{\boldsymbol{q}}^{(\tau)++}(\boldsymbol{x}^{(\tau)}) & 0 \\ 0 & n_{\boldsymbol{q}}^{(\tau)--}(\boldsymbol{x}^{(\tau)}) \end{pmatrix}\right]}, \tag{28}$$

with

$$n_{\boldsymbol{q}}^{(\tau)++}(\boldsymbol{x}^{(\tau)}) = e^{i\varphi_{l_\tau}} a_{\boldsymbol{q}}^{(\tau)++}(\boldsymbol{x}^{(\tau)}) r(\beta), \tag{29a}$$

$$n_{\boldsymbol{q}}^{(\tau)--}(\boldsymbol{x}^{(\tau)}) = e^{i\varphi_{l_\tau}} a_{\boldsymbol{q}}^{(\tau)--}(\boldsymbol{x}^{(\tau)}) r^*(\beta). \tag{29b}$$

Since the two y-simplex blocks yield identical overlaps, the sign of the total overlap is fixed by the sign of any of them.

Rotated density and pairing tensors. In the y-simplex basis, the density matrix acquires a diagonal block structure

$$\rho_{\boldsymbol{q}}^{(\tau)}(\boldsymbol{x}^{(\tau)}) = \begin{pmatrix} \rho_{\boldsymbol{q}}^{(\tau)++}(\boldsymbol{x}^{(\tau)}) & 0 \\ 0 & \rho_{\boldsymbol{q}}^{(\tau)--}(\boldsymbol{x}^{(\tau)}) \end{pmatrix}, \tag{30}$$

where

$$\rho_{\boldsymbol{q}}^{(\tau)++}(\boldsymbol{x}^{(\tau)}) = e^{i\varphi_{l_\tau}} r(\beta) v_{\boldsymbol{q}}^{(\tau)} \left[a_{\boldsymbol{q}}^{(\tau)--}(\boldsymbol{x}^{(\tau)})\right]^{-1} v_{\boldsymbol{q}}^{(\tau)\dagger}, \tag{31a}$$

$$\rho_{\boldsymbol{q}}^{(\tau)--}(\boldsymbol{x}^{(\tau)}) = e^{i\varphi_{l_\tau}} r^*(\beta) v_{\boldsymbol{q}}^{(\tau)*} \left[a_{\boldsymbol{q}}^{(\tau)++}(\boldsymbol{x}^{(\tau)})\right]^{-1} v_{\boldsymbol{q}}^{(\tau)T}. \tag{31b}$$

On the other hand, the pairing tensor acquires an off-diagonal block structure

$$\kappa_{\boldsymbol{q}}^{(\tau)}(\boldsymbol{x}^{(\tau)}) = \begin{pmatrix} 0 & \kappa_{\boldsymbol{q}}^{(\tau)+-}(\boldsymbol{x}^{(\tau)}) \\ \kappa_{\boldsymbol{q}}^{(\tau)-+}(\boldsymbol{x}^{(\tau)}) & 0 \end{pmatrix}, \tag{32}$$

where

$$\kappa_{\boldsymbol{q}}^{(\tau)+-}(\boldsymbol{x}^{(\tau)}) = -e^{i\varphi_{l_\tau}} r(\beta) v_{\boldsymbol{q}}^{(\tau)} \left[a_{\boldsymbol{q}}^{(\tau)--}(\boldsymbol{x}^{(\tau)})\right]^{-1} u_{\boldsymbol{q}}^{(\tau)\dagger}, \tag{33a}$$

$$\kappa_{\boldsymbol{q}}^{(\tau)-+}(\boldsymbol{x}^{(\tau)}) = e^{i\varphi_{l_\tau}} r^*(\beta) v_{\boldsymbol{q}}^{(\tau)*} \left[a_{\boldsymbol{q}}^{(\tau)++}(\boldsymbol{x}^{(\tau)})\right]^{-1} u_{\boldsymbol{q}}^{(\tau)T}. \tag{33b}$$

Similarly,

$$\kappa_{\boldsymbol{q}}^{*(\tau)}(\boldsymbol{x}^{(\tau)}) = \begin{pmatrix} 0 & \kappa_{\boldsymbol{q}}^{*(\tau)+-}(\boldsymbol{x}^{(\tau)}) \\ \kappa_{\boldsymbol{q}}^{*(\tau)-+}(\boldsymbol{x}^{(\tau)}) & 0 \end{pmatrix}, \tag{34}$$

with

$$\kappa_{\boldsymbol{q}}^{*(\tau)+-}(\boldsymbol{x}^{(\tau)}) = -e^{-i\varphi_{l_\tau}} r^*(\beta) u_{\boldsymbol{q}}^{(\tau)*} \left[a_{\boldsymbol{q}}^{(\tau)++}(\boldsymbol{x}^{(\tau)})\right]^{-1} v_{\boldsymbol{q}}^{(\tau)T}, \tag{35a}$$

$$\kappa_{\boldsymbol{q}}^{*(\tau)-+}(\boldsymbol{x}^{(\tau)}) = e^{-i\varphi_{l_\tau}} r(\beta) u_{\boldsymbol{q}}^{(\tau)} \left[a_{\boldsymbol{q}}^{(\tau)--}(\boldsymbol{x}^{(\tau)})\right]^{-1} v_{\boldsymbol{q}}^{(\tau)\dagger}. \tag{35b}$$

2.1.4. Making use of the symmetries

The expansion in the y-simplex basis enables us to reduce the computational cost by making all matrices block-diagonal. The computational cost can further be reduced by exploiting the symmetries in rotational angle β and gauge angle φ_{l_τ}:

- For reflection-symmetric configurations ($q_{30} = 0$), all quantities are symmetric around $\beta = \pi/2$. Consequently, the projection interval can be reduced to $\beta \in [0, \pi/2]$. This feature is automatically implemented for all reflection-symmetric configurations.
- The projection interval in gauge angle φ_{l_τ} can always be reduced to $\varphi_{l_\tau} \in [0, \pi]$ due to the number-parity symmetry of an HFB state. In addition, using symmetries of the two simplex blocks, we have

$$\mathcal{N}_{\boldsymbol{q}}^{(\tau)}(\beta, \pi - \varphi_{l_\tau}) = \left[\mathcal{N}_{\boldsymbol{q}}^{(\tau)}(\beta, \varphi_{l_\tau})\right]^*, \tag{36a}$$

$$\rho_{\boldsymbol{q}}^{(\tau)++}(\beta, \pi - \varphi_{l_\tau}) = \left[\rho_{\boldsymbol{q}}^{(\tau)--}(\beta, \varphi_{l_\tau})\right]^*, \tag{36b}$$

$$\rho_{\boldsymbol{q}}^{(\tau)--}(\beta, \pi - \varphi_{l_\tau}) = \left[\rho_{\boldsymbol{q}}^{(\tau)++}(\beta, \varphi_{l_\tau})\right]^*, \tag{36c}$$

$$\kappa_{\boldsymbol{q}}^{(\tau)+-}(\beta, \pi - \varphi_{l_\tau}) = -[\kappa_{\boldsymbol{q}}^{(\tau)-+}(\beta, \varphi_{l_\tau})]^*, \tag{36d}$$

$$\kappa_{\boldsymbol{q}}^{(\tau)-+}(\beta, \pi - \varphi_{l_\tau}) = -\left[\kappa_{\boldsymbol{q}}^{(\tau)+-}(\beta, \varphi_{l_\tau})\right]^*, \tag{36e}$$

$$\kappa_{\boldsymbol{q}}^{*(\tau)+-}(\beta, \pi - \varphi_{l_\tau}) = -[\kappa_{\boldsymbol{q}}^{*(\tau)-+}(\beta, \varphi_{l_\tau})]^*, \tag{36f}$$

$$\kappa_{\boldsymbol{q}}^{*(\tau)-+}(\beta, \pi - \varphi_{l_\tau}) = -\left[\kappa_{\boldsymbol{q}}^{*(\tau)+-}(\beta, \varphi_{l_\tau})\right]^*. \tag{36g}$$

  Consequently, only quantities within the interval $\varphi_{l_\tau} \in [0, \pi/2]$ are explicitly calculated.

2.1.5. Densities in the coordinate-space representation

The expressions (18a) - (18c) for the rotated (transition) density and pairing tensors are written in the configuration space, that is, the quantities $U_{\boldsymbol{q}}^{(\tau)}$, $V_{\boldsymbol{q}}^{(\tau)}$, etc., are matrices. When using Skyrme EDFs, the coordinate-space representation is also especially useful.

General expressions. In the coordinate-space representation, the full one-body density matrix for particle type τ can be written as

$$\begin{aligned}\rho_{\boldsymbol{q}}^{(\tau)}(\boldsymbol{r}\sigma, \boldsymbol{r}'\sigma') = &\frac{1}{2}\rho_{\boldsymbol{q}}^{(\tau)}(\boldsymbol{r}, \boldsymbol{r}')\delta_{\sigma\sigma'} \\ &+ \frac{1}{2}\sum_{\mu} \langle\sigma|\hat{\sigma}_\mu|\sigma'\rangle\, s_{\boldsymbol{q},\mu}^{(\tau)}(\boldsymbol{r}, \boldsymbol{r}'),\end{aligned} \tag{37}$$

where $\rho_{\boldsymbol{q}}^{(\tau)}(\boldsymbol{r}, \boldsymbol{r}')$ is the non-local one-body particle density

$$\rho_{\boldsymbol{q}}^{(\tau)}(\boldsymbol{r}, \boldsymbol{r}') = \sum_{\sigma} \rho_{\boldsymbol{q}}^{(\tau)}(\boldsymbol{r}\sigma, \boldsymbol{r}'\sigma) \tag{38}$$

and $s_{\boldsymbol{q},\mu}^{(\tau)}(\boldsymbol{r}, \boldsymbol{r}')$ is the μ component of the non-local one-body spin density

$$s_{\boldsymbol{q},\mu}^{(\tau)}(\boldsymbol{r}, \boldsymbol{r}') = \sum_{\sigma\sigma'} \rho_{\boldsymbol{q}}^{(\tau)}(\boldsymbol{r}\sigma, \boldsymbol{r}'\sigma')\, \langle\sigma'|\sigma_\mu|\sigma\rangle\,. \tag{39}$$

These non-local densities can be used to generate an auxiliary set of local densities that will appear in the expression for the energy density functional. In particular, the local particle density $\rho_{\boldsymbol{q}}^{(\tau)}(\boldsymbol{r})$, the local spin density $\boldsymbol{s}_{\boldsymbol{q}}^{(\tau)}(\boldsymbol{r})$, the kinetic energy density $\tau_{\boldsymbol{q}}^{(\tau)}(\boldsymbol{r})$, the spin kinetic energy density $\boldsymbol{T}_{\boldsymbol{q}}^{(\tau)}(\boldsymbol{r})$, the current density $\boldsymbol{j}_{\boldsymbol{q}}^{(\tau)}(\boldsymbol{r})$, and the spin current density $\mathrm{J}_{\boldsymbol{q}}^{(\tau)}(\boldsymbol{r})$ read

$$\rho_{\boldsymbol{q}}^{(\tau)}(\boldsymbol{r}) = \rho_{\boldsymbol{q}}^{(\tau)}(\boldsymbol{r},\boldsymbol{r}), \tag{40a}$$
$$\boldsymbol{s}_{\boldsymbol{q}}^{(\tau)}(\boldsymbol{r}) = \boldsymbol{s}_{\boldsymbol{q}}^{(\tau)}(\boldsymbol{r},\boldsymbol{r}), \tag{40b}$$
$$\tau_{\boldsymbol{q}}^{(\tau)}(\boldsymbol{r}) = \nabla\cdot\nabla'\rho_{\boldsymbol{q}}^{(\tau)}(\boldsymbol{r},\boldsymbol{r}')|_{\boldsymbol{r}'=\boldsymbol{r}}, \tag{40c}$$
$$T_{\boldsymbol{q},\mu}^{(\tau)}(\boldsymbol{r}) = \nabla\cdot\nabla' s_{\boldsymbol{q},\mu}^{(\tau)}(\boldsymbol{r},\boldsymbol{r}')|_{\boldsymbol{r}'=\boldsymbol{r}}, \tag{40d}$$
$$\boldsymbol{j}_{\boldsymbol{q}}^{(\tau)}(\boldsymbol{r}) = \frac{1}{2i}(\nabla-\nabla')\rho_{\boldsymbol{q}}^{(\tau)}(\boldsymbol{r},\boldsymbol{r}')|_{\boldsymbol{r}'=\boldsymbol{r}}, \tag{40e}$$
$$J_{\boldsymbol{q},\mu\nu}^{(\tau)}(\boldsymbol{r}) = \frac{1}{2i}(\nabla_\mu-\nabla'_\mu)s_{\boldsymbol{q},\nu}^{(\tau)}(\boldsymbol{r},\boldsymbol{r}')|_{\boldsymbol{r}'=\boldsymbol{r}},. \tag{40f}$$

Furthermore, the non-local pairing densities for particle type τ are defined through the corresponding pairing tensors as

$$\tilde{\rho}_{\boldsymbol{q}}^{(\tau)}(\boldsymbol{r}\sigma,\boldsymbol{r}'\sigma') = (-2\sigma')\kappa_{\boldsymbol{q}}^{(\tau)}(\boldsymbol{r}\sigma,\boldsymbol{r}'-\sigma'), \tag{41a}$$
$$\tilde{\rho}_{\boldsymbol{q}}^{*(\tau)}(\boldsymbol{r}\sigma,\boldsymbol{r}'\sigma') = (-2\sigma')\kappa_{\boldsymbol{q}}^{*(\tau)}(\boldsymbol{r}\sigma,\boldsymbol{r}'-\sigma'). \tag{41b}$$

They can be equivalently expanded as

$$\tilde{\rho}_{\boldsymbol{q}}^{(\tau)}(\boldsymbol{r}\sigma,\boldsymbol{r}'\sigma') = \frac{1}{2}\tilde{\rho}_{\boldsymbol{q}}^{(\tau)}(\boldsymbol{r},\boldsymbol{r}')\delta_{\sigma\sigma'} + \frac{1}{2}\sum_\mu \langle\sigma|\hat{\sigma}_\mu|\sigma'\rangle\,\tilde{s}_{\boldsymbol{q},\mu}^{(\tau)}(\boldsymbol{r},\boldsymbol{r}'). \tag{42}$$

However, only local pairing densities will be considered in the pairing term of the energy density functional

$$\tilde{\rho}_{\boldsymbol{q}}^{(\tau)}(\boldsymbol{r}) = \tilde{\rho}_{\boldsymbol{q}}^{(\tau)}(\boldsymbol{r},\boldsymbol{r}), \tag{43a}$$
$$\tilde{\rho}_{\boldsymbol{q}}^{*(\tau)}(\boldsymbol{r}) = \tilde{\rho}_{\boldsymbol{q}}^{*(\tau)}(\boldsymbol{r},\boldsymbol{r}). \tag{43b}$$

Formally, equations (40a) - (40f) and (43a) - (43b) look identical regardless of whether $\rho_{\boldsymbol{q}}^{(\tau)}(\boldsymbol{r}\sigma,\boldsymbol{r}'\sigma')$ is the diagonal one-body density matrix,

$$\rho_{\boldsymbol{q}}^{(\tau)}(\boldsymbol{r}\sigma,\boldsymbol{r}'\sigma') \equiv \frac{\langle\Phi_{\boldsymbol{q}}|c^\dagger(\boldsymbol{r}'\sigma'\tau)c(\boldsymbol{r}\sigma\tau)|\Phi_{\boldsymbol{q}}\rangle}{\langle\Phi_{\boldsymbol{q}}|\Phi_{\boldsymbol{q}}\rangle} \tag{44}$$

or the rotated (transition) one-body density,

$$\rho_{\boldsymbol{q}}^{(\tau)}(\boldsymbol{r}\sigma,\boldsymbol{r}'\sigma';\eta) \equiv \frac{\langle\Phi_{\boldsymbol{q}}|c^\dagger(\boldsymbol{r}'\sigma'\tau)c(\boldsymbol{r}\sigma\tau)\mathcal{R}[\eta]|\Phi_{\boldsymbol{q}}\rangle}{\langle\Phi_{\boldsymbol{q}}|\mathcal{R}[\eta]|\Phi_{\boldsymbol{q}}\rangle}, \tag{45}$$

where $c^\dagger(\boldsymbol{r}'\sigma'\tau)$ and $c(\boldsymbol{r}\sigma\tau)$ are the creation and the annihilation operator for particle τ corresponding to the single-particle basis of choice, $\mathcal{R}$ is the transformation (rotation) operator related to the symmetry being restored, and η denotes a set of real numbers parametrizing the elements of the symmetry group(s) related to the transformation $\mathcal{R}$ (that is, in our case, $\eta \equiv \boldsymbol{x}^{(\tau)}$). The main difference is that for diagonal one-body density matrix all local densities are real-valued if axial-symmetry is enforced. On the other hand, the densities stemming from the latter matrix are generally complex-valued [33]. For completeness, we give the explicit expressions for the densities and currents (40a) - (40f) and (43a) - (43b) in Appendix A.

Time-odd densities and symmetry restoration. Within the HFB theory, the local densities $\rho_{\boldsymbol{q}}^{(\tau)}$, $\tau_{\boldsymbol{q}}^{(\tau)}$, and $J_{\boldsymbol{q}}^{(\tau)}$ are even, while $\boldsymbol{s}_{\boldsymbol{q}}^{(\tau)}$, $\boldsymbol{T}_{\boldsymbol{q}}^{(\tau)}$, and $\boldsymbol{j}_{\boldsymbol{q}}^{(\tau)}$ are odd under the time-reversal transformation [34]. When the HFB state $|\Phi_{\boldsymbol{q}}\rangle$ in (44) is time-even, as is the case for even-even nuclei at the SR-EDF level, the $\rho_{\boldsymbol{q}}^{(\tau)}(\boldsymbol{r}\sigma,\boldsymbol{r}'\sigma')$ matrix is time-even as well. Consequently, one can show that in such cases $\boldsymbol{s}_{\boldsymbol{q}}^{(\tau)}(\boldsymbol{r}) = \boldsymbol{T}_{\boldsymbol{q}}^{(\tau)}(\boldsymbol{r}) = \boldsymbol{j}_{\boldsymbol{q}}^{(\tau)}(\boldsymbol{r}) = 0$ and the corresponding energy contributions vanish identically. Furthermore, blocking calculations for odd nuclei in HFBTHO are implemented in the equal filling approximation [35], which enforces the conservation of time-reversal symmetry. Therefore, the time-odd densities do not contribute in this case either.

However, the situation is generally different for transition densities of Eq. (45), such as the gauge- and Euler-rotated densities appearing at the MR-EDF level [33]. Most importantly, the transition densities are generally not Hermitian. Consequently, even if the HFB state is time-even, the time-odd densities and the corresponding energy contributions may not vanish identically. In the particular case of particle number projection (PNP), one can show that the one-body density matrix is symmetric in the oscillator basis and that, as a result, the spin density transforms under the time-reversal as $\hat{T}\boldsymbol{s}_{\boldsymbol{q},\mu}^{(\tau)}(\boldsymbol{r},\boldsymbol{r}') = -\boldsymbol{s}_{\boldsymbol{q},\mu}^{(\tau)}(\boldsymbol{r},\boldsymbol{r}')$. This property ensures that the spin density vanishes identically when the reference state is time-even. However, this result is specific to the case of PNP alone. For the angular momentum projection (AMP) or the combined PNP and AMP, all time-odd densities are generally non-zero and contribute to the projected energy (or any other observable).

2.1.6. Rotated energy density functional

Rotated Hamiltonian kernel. The rotated Hamiltonian kernel is a functional of the rotated density and rotated pairing tensors. It corresponds to a spatial integral of the rotated energy density functional

$$\mathcal{H}_{\boldsymbol{q}}(\boldsymbol{x})[\rho,\kappa,\kappa^*] = \int d^3\boldsymbol{r}\,\mathcal{E}_{\boldsymbol{q}}(\boldsymbol{r};\boldsymbol{x})[\rho,\kappa,\kappa^*], \tag{46}$$

where $\boldsymbol{x} \equiv \{\boldsymbol{x}^{(\tau=n)},\boldsymbol{x}^{(\tau=p)}\}$. Version 4.0 of HFBTHO implements the restoration of symmetries for Skyrme-based EDFs only.

The total EDF can be decomposed into the particle-hole (Skyrme) part and the particle-particle (pairing) part

$$\mathcal{E}_{\boldsymbol{q}}(\boldsymbol{r};\boldsymbol{x}) = \mathcal{E}_{\boldsymbol{q}}^{\text{Sky}}(\boldsymbol{r};\boldsymbol{x}) + \mathcal{E}_{\boldsymbol{q}}^{\text{pair}}(\boldsymbol{r};\boldsymbol{x}), \tag{47}$$

where

$$\mathcal{E}_{\boldsymbol{q}}^{\text{Sky}}(\boldsymbol{r};\boldsymbol{x}) = \mathcal{E}_{\boldsymbol{q}}^{\text{kin}}(\boldsymbol{r};\boldsymbol{x}) + \mathcal{E}_{\boldsymbol{q}}^{\text{Cou}}(\boldsymbol{r};\boldsymbol{x}) + \mathcal{E}_{\boldsymbol{q}}^{\text{pot}}(\boldsymbol{r};\boldsymbol{x}). \tag{48}$$

Note that functional dependencies on the rotated density and pairing tensors were dropped for compactness on each side of Eqs. (47) and (48). The kinetic term simply reads

$$\mathcal{E}_{\boldsymbol{q}}^{\text{kin}}(\boldsymbol{r};\boldsymbol{x}) = \sum_{\tau=n,p}\frac{\hbar^2}{2m}\tau_{\boldsymbol{q}}^{(\tau)}(\boldsymbol{r};\boldsymbol{x}). \tag{49a}$$

The Coulomb term can be decomposed into the direct and the exchange part, $\mathcal{E}_{\boldsymbol{q}}^{\text{Cou}}(\boldsymbol{r};\boldsymbol{x}) = \mathcal{E}_{\boldsymbol{q}}^{\text{Cou,dir}}(\boldsymbol{r};\boldsymbol{x}) + \mathcal{E}_{\boldsymbol{q}}^{\text{Cou,exc}}(\boldsymbol{r};\boldsymbol{x})$. The direct contribution is calculated as

$$\mathcal{E}_{\boldsymbol{q}}^{\text{Cou,dir}}(\boldsymbol{r};\boldsymbol{x}) = \frac{1}{2}\int d^3\boldsymbol{r}'\frac{\rho_{\boldsymbol{q}}^{(p)}(\boldsymbol{r};\boldsymbol{x})\rho_{\boldsymbol{q}}^{(p)}(\boldsymbol{r}')}{|\boldsymbol{r}-\boldsymbol{r}'|}, \tag{50}$$

while the exchange contribution is calculated in the local Slater approximation and the Coulomb potential is computed with the non-rotated density to save computational time. The resulting error is less than 100 keV on the $J = 10$ state of Table 2.

$$\mathcal{E}_{\boldsymbol{q}}^{\text{Cou,exc}}(\boldsymbol{r};\boldsymbol{x}) = -\frac{3e^2}{4}\left(\frac{3}{\pi}\right)^{1/3}\left[\rho_{\boldsymbol{q}}^{(p)}(\boldsymbol{r};\boldsymbol{x})\right]^{4/3}. \tag{51}$$

Note that the pairing contribution of the Coulomb interaction has been omitted.

Furthermore, the Skyrme pseudopotential term can also be decomposed into two contributions

$$\mathcal{E}_{\boldsymbol{q}}^{\text{pot}}(\boldsymbol{r};\boldsymbol{x}) = \sum_{t=0,1}\left[\mathcal{E}_{\boldsymbol{q},t}^{\text{pot,even}}(\boldsymbol{r};\boldsymbol{x}) + \mathcal{E}_{\boldsymbol{q},t}^{\text{pot,odd}}(\boldsymbol{r};\boldsymbol{x})\right], \tag{52}$$

where the former is built from time-even densities and currents only, while the latter is built from time-odd densities and currents only. Of course, both contributions are themselves time-even by construction. Furthermore, the summation over t in Eq. (52) reflects the coupling of neutron and proton densities and currents into the isoscalar ($t=0$) and the isovector ($t=1$) channel, i.e.

$$\begin{aligned}\rho_{\boldsymbol{q},0}(\boldsymbol{r};\boldsymbol{x}) &= \rho^{(n)}_{\boldsymbol{q}}(\boldsymbol{r};\boldsymbol{x}) + \rho^{(p)}_{\boldsymbol{q}}(\boldsymbol{r};\boldsymbol{x}),\\ \rho_{\boldsymbol{q},1}(\boldsymbol{r};\boldsymbol{x}) &= \rho^{(n)}_{\boldsymbol{q}}(\boldsymbol{r};\boldsymbol{x}) - \rho^{(p)}_{\boldsymbol{q}}(\boldsymbol{r};\boldsymbol{x}),\end{aligned} \tag{53}$$

and equivalently for other densities and currents. The time-even contribution to the EDF then reads

$$\begin{aligned}\mathcal{E}^{\text{pot,even}}_{\boldsymbol{q},t}(\boldsymbol{r};\boldsymbol{x}) = {}& C^{\rho\rho}_{\boldsymbol{q},t}(\boldsymbol{r};\boldsymbol{x})\rho^2_{\boldsymbol{q},t}(\boldsymbol{r};\boldsymbol{x})\\ &+ C^{\rho\Delta\rho}_{t}\rho_{\boldsymbol{q},t}(\boldsymbol{r};\boldsymbol{x})\Delta\rho_{\boldsymbol{q},t}(\boldsymbol{r};\boldsymbol{x})\\ &+ C^{\rho\tau}_{t}\rho_{\boldsymbol{q},t}(\boldsymbol{r};\boldsymbol{x})\tau_{\boldsymbol{q},t}(\boldsymbol{r};\boldsymbol{x})\\ &+ C^{\rho\nabla J}_{t}\rho_{\boldsymbol{q},t}(\boldsymbol{r};\boldsymbol{x})\nabla\cdot\boldsymbol{J}_{\boldsymbol{q},t}(\boldsymbol{r};\boldsymbol{x})\\ &+ C^{JJ}_{t}\sum_{\mu\nu}J_{\boldsymbol{q},t,\mu\nu}(\boldsymbol{r};\boldsymbol{x})J_{\boldsymbol{q},t,\mu\nu}(\boldsymbol{r};\boldsymbol{x}),\end{aligned} \tag{54}$$

and the time-odd contribution reads

$$\begin{aligned}\mathcal{E}^{\text{pot,odd}}_{\boldsymbol{q},t}(\boldsymbol{r};\boldsymbol{x}) = {}& C^{ss}_{\boldsymbol{q},t}(\boldsymbol{r};\boldsymbol{x})\boldsymbol{s}^2_{\boldsymbol{q},t}(\boldsymbol{r};\boldsymbol{x})\\ &+ C^{s\Delta s}_{t}\boldsymbol{s}_{\boldsymbol{q},t}(\boldsymbol{r};\boldsymbol{x})\Delta\boldsymbol{s}_{\boldsymbol{q},t}(\boldsymbol{r};\boldsymbol{x})\\ &+ C^{sj}_{t}\boldsymbol{j}^2_{\boldsymbol{q},t}(\boldsymbol{r};\boldsymbol{x})\\ &+ C^{s\nabla j}_{t}\boldsymbol{s}_{\boldsymbol{q},t}(\boldsymbol{r};\boldsymbol{x})\cdot\Big(\nabla\times\boldsymbol{j}_{\boldsymbol{q},t}(\boldsymbol{r};\boldsymbol{x})\Big)\\ &+ C^{sT}_{t}\boldsymbol{s}_{\boldsymbol{q},t}(\boldsymbol{r};\boldsymbol{x})\cdot\boldsymbol{T}_{\boldsymbol{q},t}(\boldsymbol{r};\boldsymbol{x}).\end{aligned} \tag{55}$$

Note that the coupling constants $C^{\rho\rho}_{\boldsymbol{q},t}(\boldsymbol{r};\boldsymbol{x})$ and $C^{ss}_{\boldsymbol{q},t}(\boldsymbol{r};\boldsymbol{x})$ are density-dependent. Furthermore, the last terms in Eqs. (54) and (55) represent tensor contributions and are set to zero by construction in a number of Skyrme EDFs. The full expressions for coupling constants C_t in terms of the (t,x) parameters of the Skyrme EDF are given in Appendix B.

Finally, the pairing term reads

$$\mathcal{E}^{\text{pair}}_{\boldsymbol{q}}(\boldsymbol{r};\boldsymbol{x}) = \sum_{\tau=n,p}C^{\text{pair}(\tau)}_{\boldsymbol{q}}(\boldsymbol{r},\boldsymbol{x})\tilde{\rho}^{(\tau)}_{\boldsymbol{q}}(\boldsymbol{r};\boldsymbol{x})\tilde{\rho}^{*(\tau)}_{\boldsymbol{q}}(\boldsymbol{r};\boldsymbol{x}), \tag{56}$$

with

$$C^{\text{pair}(\tau)}_{\boldsymbol{q}}(\boldsymbol{r},\boldsymbol{x}) = \frac{V^{(\tau)}_0}{4}\left[1-V^{(\tau)}_1\left(\frac{\rho_{\boldsymbol{q}}(\boldsymbol{r};\boldsymbol{x})}{\rho_c}\right)\right], \tag{57}$$

where $V^{(\tau)}_0$ is the pairing strength for particle τ, $V^{(\tau)}_1$ controls the nature of pairing between the pure volume ($V^{(\tau)}_1=0$) and the pure surface ($V^{(\tau)}_1=1$) interaction, and $\rho_c=0.16$ fm^{-3} is the saturation density of nuclear matter.

Rotated Hamiltonian kernel of density-dependent terms. Nearly all parameterizations of Skyrme and Gogny EDFs include a density-dependent two-body term. This term has a strongly repulsive character and was originally introduced to reproduce the saturation property of the nuclear interaction. However, since it is not linked to a genuine Hamiltonian operator, its contribution to the rotated Hamiltonian kernel is ambiguous. In fact, this contribution can be determined only by introducing an additional prescription [36,37]. The choice of prescription will influence the calculated projected energies and can therefore be considered as yet another parameter of a density-dependent EDF.

A common choice is the *mixed density* prescription

$$\rho^{(\tau)}_{\boldsymbol{q},\text{mix}}(\boldsymbol{r};\beta,\varphi_{l_\tau}) = \frac{\langle\Phi_{\boldsymbol{q}}|\hat{\rho}^{(\tau)}(\boldsymbol{r})e^{-i\beta\hat{J}_y}e^{i\varphi_{l_\tau}\hat{\tau}}|\Phi_{\boldsymbol{q}}\rangle}{\langle\Phi_{\boldsymbol{q}}|\Phi_{\boldsymbol{q}}\rangle}, \tag{58}$$

where $\hat{\rho}^{(\tau)}(\boldsymbol{r})$ is the one-body density operator for particle type τ at point $\boldsymbol{r}$. This prescription is motivated by the expression for the Hamiltonian kernel of density-independent interactions based on the generalized Wick theorem. Moreover, it is the only prescription on the market satisfying all the consistency requirements [36]. Most importantly, even though the mixed density (58) is generally complex, the resulting projected energies are always real and invariant under symmetry transformations. Nevertheless, if a density-dependent term contains a non-integer power of density, the corresponding energy contribution is generally ill-defined. This issue is essentially insurmountable and can be circumvented only by using density-dependent terms with integer powers of density or a different density prescription. A possible alternative is the *projected density* prescription

$$\rho^{(\tau)}_{\boldsymbol{q},\text{proj}}(\boldsymbol{r};\beta) = \frac{\langle\Phi_{\boldsymbol{q}}|\hat{\rho}^{(\tau)}(\boldsymbol{r})e^{-i\beta\hat{J}_y}\hat{P}^X|\Phi_{\boldsymbol{q}}\rangle}{\langle\Phi_{\boldsymbol{q}}|e^{-i\beta\hat{J}_y}\hat{P}^X|\Phi_{\boldsymbol{q}}\rangle}, \tag{59}$$

which is real by construction. Unfortunately, it yields non-physical results when used in restoration of spatial symmetries, such as the rotational or reflection symmetry [37]. Nevertheless, a hybrid approach is possible in which the mixed density prescription is used when restoring spatial symmetries, while the projected density prescription is used when restoring the particle number symmetry. Such an approach has been routinely employed in MR-EDF calculations with Gogny EDFs by the Madrid group [4].

The Skyrme EDFs included in the current implementation contain two density-dependent terms: (i) the volume term proportional to $\rho^\alpha(\boldsymbol{r})$, where α can be either integer or non-integer depending on the EDF, and (ii) the Coulomb exchange term proportional to $[\rho^{(p)}(\boldsymbol{r})]^{4/3}$. In addition, the pairing interaction is proportional to $\rho(\boldsymbol{r})$, except in the case of the pure volume pairing. The version 4.0 of HFBTHO implements the mixed density prescription in restoration of the rotational, reflection, and particle number symmetry. However, the code enables choosing the projected density prescription in particle number projection for the volume term with non-integer α and the Coulomb exchange term.

2.2. HFBTHO library

The code source has been largely refactored to facilitate maintenance and future developments. This refactoring included modularizing the code base, removing obsolescent Fortran statements, and generalizing Fortran 2003 constructs. In each module, module variables, functions, and subroutines are thus explicitly declared as `private` and `public`. Furthermore, arguments passed to each function and subroutine have the `intent(in/out/inout)` attribute. The internal structure of the code has also been reorganized in order to produce an HFBTHO library.

Compiling the program generates the following three objects:

- A Fortran executable called `hfbtho_main`. The call sequence of the program has been modified to provide more flexibility while maintaining backward compatibility; refer to Sec. 5.2 for a short description.
- A static library `libhfbtho.a`. This library provides, among others, the routine `Main_Program()` with the following call sequence

```
Subroutine Main_Program(
   filename_hfbtho,filename_unedf, &
   my_comm_world,my_comm_team, &
   my_n_teams,my_team_color, &
   toggle_output,filename_output, &
   filename_dat,filename_binary)
```

This routine will execute a full HFBTHO calculation, possibly across different MPI ranks. Its arguments are the following:
- `filename_hfbtho`: the name of the input data file containing the Namelists.
  Default: `hfbtho_NAMELIST.dat`;
- `filename_unedf`: the name of the input data file containing the parameters of the EDF.
  Default: `hfbtho_UNEDF.dat`;
- `my_comm_world`: the MPI world communicator, typically `MPI_COMM_WORLD`. When compiling the code without MPI support (`USE_MPI = 0`), this argument is inactive;
- `my_comm_team`: the MPI communicator used to break the MPI processes into teams, each of which handles a given HFBTHO calculation. Currently, distributed parallelism through MPI is only used when restoring broken symmetries. Without MPI support, this argument is inactive;
- `my_n_teams`: the number of teams in the calculation. Without MPI support, this argument is inactive;
- `my_team_color`: the team "color" of the MPI process, i.e., the unique ID number of the team to which the process has been assigned. Without MPI support, this argument is inactive;
- `toggle_output`: if equal to 0, then no ASCII output is recorded on file; if equal to 1, the two files `filename_output` and `filename_dat` described below are written on disk;
- `filename_output`: the name of the ASCII output file where the results of the calculation are written.
  Default: `hfbtho.out`;
- `filename_dat`: the name of the ASCII output file where extended results of the calculations are written. Extended results include the self-consistent loop, observables, quasiparticle energies, equivalent single-particle energies, and Nilsson labels.
  Default: `thoout.dat`;
- `filename_binary`: the name of the binary file where the code will store the data needed to restart the iterations.
  Default: `hfbtho_output.hel`.

- A Python3 binding. The precise name of the binding will depend on the user's system, the Python version, and the Fortran compiler. Assuming the binding is (re)named `hfbtho_library.so`, it can be used directly from a Python environment and provides access to the `Main_Program()` routine. For example:

```
from hfbtho_library import Main_Program
```

or

```
import hfbtho_library
```

2.3. Other changes

SeaLL1 functional. The SeaLL1 EDF [38] is now available in the code. As a reminder, this functional reads

$$\begin{aligned}\mathcal{E}_{\text{SeaLL1}}(\boldsymbol{r}) &= \frac{\hbar^2}{2m}\left(\tau^{(n)}(\boldsymbol{r})+\tau^{(p)}(\boldsymbol{r})\right)\\ &+\sum_{j=0}^{2}\left(a_j\rho_0^{5/3}(\boldsymbol{r})+b_j\rho_0^{2}(\boldsymbol{r})+c_j\rho_0^{7/3}(\boldsymbol{r})\right)\beta^{2j}\\ &+\eta_s\sum_{\tau=n,p}\frac{\hbar^2}{2m}|\nabla\rho^{(\tau)}(\boldsymbol{r})|^2+W_0\ \boldsymbol{J}_0(\boldsymbol{r})\cdot\nabla\rho_0(\boldsymbol{r})\\ &+\frac{e^2}{2}\int d^3\boldsymbol{r}'\frac{\rho^{(p)}(\boldsymbol{r})\rho^{(p)}(\boldsymbol{r}')}{|\boldsymbol{r}-\boldsymbol{r}'|}-\frac{3e^2}{4}\left(\frac{\rho^{(p)}(\boldsymbol{r})}{3\pi}\right)^{4/3}\\ &+\sum_{\tau=n,p}g_{\text{eff}}^{(\tau)}(\boldsymbol{r})|\tilde{\rho}^{(\tau)}(\boldsymbol{r})|^2.\end{aligned} \tag{60}$$

The quantity $g_{\text{eff}}^{(\tau)}(\boldsymbol{r})$ is the renormalized pairing strength which is obtained after regularizing a volume pairing interaction of the form $g^{(\tau)}(\boldsymbol{r})=g^{(\tau)}$ [39,40]; see [5] for details about the implementation of the regularization procedure. The SeaLL1 EDF is fully characterized by 11 parameters ($\{a_j,b_j,c_j\}_{j=0,1,2},\eta_s,W_0$) in the pairing channel and 2 parameters in the particle-particle channel ($g^{(n)}$ and $g^{(p)}$, with $g^{(n)}=g^{(p)}=g_0$ for SeaLL1). Note that, like the UNEDFn functionals, SeaLL1 specifies both the particle-hole and the pairing channel.

Exact Coulomb. In previous versions of HFBTHO, the direct (Hartree) term of the Coulomb potential is calculated using the substitution method [41], the exchange (Fock) term is calculated at the Slater approximation, while the pairing term is neglected. As discussed extensively in [12], the substitution method can be numerically unstable because of aliasing errors. In the current version, we have leveraged the capability to compute mean-field and pairing energies from finite-range two-body Gaussian potentials introduced in version 3.00 to implement an "exact" calculation of the direct, exchange, and pairing term of the Coulomb potential. In particular, we follow the technique implemented in [42] and discussed in [43] and by exploiting the identity

$$\begin{aligned}\frac{1}{r}&=\frac{2}{\sqrt{\pi}}\int_0^{+\infty}d\alpha\, e^{-\alpha^2r^2}\\ &=\frac{2}{L\sqrt{\pi}}\int_0^{1}d\xi\,(1-\xi^2)^{-3/2}\exp\left(-\frac{\xi^2r^2}{L^2(1-\xi^2)}\right),\end{aligned} \tag{61}$$

where we used the change of variable $\alpha=\frac{\xi}{L}(1-\xi^2)^{-1/2}$ and L stands for the larger of the two oscillator lengths, $L=\max(b_z,b_\perp)$. The second integral can be efficiently computed with Gauss-Legendre quadrature. If ω_i and ξ_i are the weights and the nodes of Gauss-Legendre quadrature, then we can write

$$\frac{1}{r}=\sum_{i=1}^{N_c}A_ie^{-a_ir^2}, \tag{62}$$

with $A_i=\frac{2\omega_i}{L\sqrt{\pi}}(1-\xi_i^2)^{-3/2}$ and $a_i=\frac{\xi_i^2}{L^2(1-\xi_i^2)}$.

Overwrite mode. The new version of the code provides an option to use the information contained in the binary `hfbtho_output.hel` file to overwrite some of the user-defined inputs. This option is activated by setting the energy functional to `READ` (instead of the usual `SLY4`, `SKM*`, etc.). In this case, the code will overwrite (i) all the parameters of the EDF, (ii) the pairing cutoff, (iii) the activation/deactivation of non-standard terms such as the center-of-mass correction, tensor terms, or pairing regularization, (iv) the parameters of the oscillator basis such as the maximal number of shells and oscillator lengths. The code will then redefine the full HO basis to be consistent with the one on file.

Bugfix of blocking calculations. In all versions of HFBTHO since 2.00d [12], there is a bug in the calculations of blocked states when the "automatic" mode is activated. In this mode, the code determines and computes all possible blocking configurations within a 2 MeV

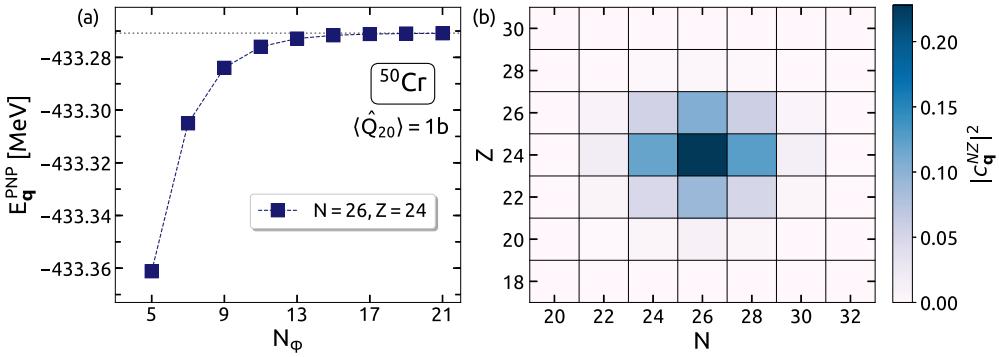

Fig. 1. Particle number projection in the quasiparticle basis for the $\langle\hat{Q}_{20}\rangle = 1$ b configuration in ^{50}Cr. (a): The PNP energy as a function of the number of gauge angles N_φ. The dashed horizontal line denotes the fully converged solution ($N_\varphi = 99$). (b): The decomposition of an HFB state onto different numbers of neutrons and protons for $N_\varphi = 15$. (For interpretation of the colors in the figure(s), the reader is referred to the web version of this article.)

energy window around the Fermi level; see Section 4.2 of [12] for details. In practice, the code loops over all N candidate configurations. Occasionally, one of these configurations may diverge, e.g., the particle number condition cannot be enforced. When this happened to a configuration $1 \leq k < N$, the code would simply exit the loop without trying to compute the remaining configurations $k < k' \leq N$. Consequently, the results of the converged calculations were correct but some potentially valid configurations were not computed. In calculations near the ground state of stable nuclei, this situation occurs very rarely; in calculations of very neutron-rich or very deformed nuclei, it may happen more frequently. This bug is fixed in the current version of the code.

3. Benchmarks and accuracy

3.1. Particle number projection

As the first illustrative example, we perform the particle number projection for a range of quadrupole-deformed configurations in ^{50}Cr. Well-converged solutions are obtained by expanding the HFB states in a spherical HO basis with $N_0 = 8$ shells and the oscillator length $b_0 = 1.7621858$ fm. The SIII parametrization of the Skyrme EDF [44] is used, alongside a volume ($V_1^{(\tau)} = 0.0$) contact pairing interaction [39] with a 60 MeV quasiparticle cutoff and pairing strengths $V_0^{(n)} = V_0^{(p)} = -190.0$ MeV. In addition, we employ the mixed density prescription.

3.1.1. Convergence and particle number decomposition

We start by testing the convergence of PNP energies [$E^{\rm PNP}_{\mathbf{q}} \equiv E^{NZ}_{\mathbf{q}}$, Eq. (14)] and decomposing an HFB state onto different numbers of neutrons and protons [$|c^{NZ}_{\mathbf{q}}|^2$, Eq. (12)]. The quadrupole moment of the reference HFB state is constrained to $\langle\hat{Q}_{20}\rangle = 1$ b, the dipole and the octupole moment are constrained to zero, while higher multipole moments are determined self-consistently. Fig. 1(a) shows the corresponding PNP energy as a function of the number of gauge angles N_φ. An excellent agreement with the fully converged solution (represented by the dashed horizontal line and computed for $N_\varphi = 99$) is obtained for $N_\varphi = 15$. The convergence pattern will generally vary for different HFB states, but at most $N_\varphi = 15$ gauge angles should be sufficient for most practical purposes.

Furthermore, Fig. 1(b) shows the decomposition of the same HFB state onto different numbers of neutrons and protons. A pronounced maximum is found at the correct number of particles, $|c^{N=26,Z=24}_{\mathbf{q}}|^2 = 0.2278$. Around this point, the distribution drops sharply in all directions. For example, the configuration with two protons less has about twice smaller coefficient, $|c^{N=26,Z=22}_{\mathbf{q}}|^2 = 0.1197$, while the configuration with four protons less has only $|c^{N=26,Z=20}_{\mathbf{q}}|^2 = 0.0201$. Note that, for this particular configuration, the pairing gaps are $\Delta_n = 1.0901$ MeV and $\Delta_p = 1.1773$ MeV for neutrons and protons, respectively.

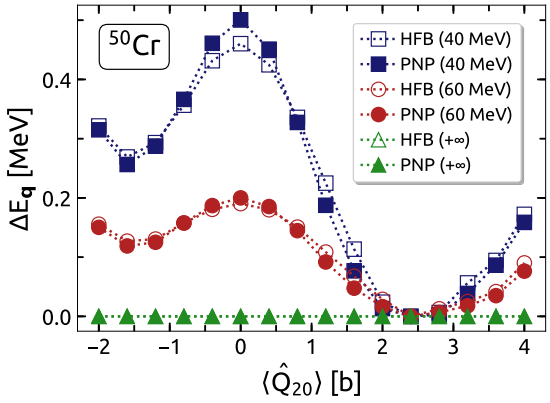

Fig. 2. The difference between the PNP energies obtained in the quasiparticle and in the canonical basis, $\Delta E^{\rm PNP}_{\mathbf{q}} = E^{\rm PNP}_{\mathbf{q},\rm qps} - E^{\rm PNP}_{\mathbf{q},\rm can}$, for three different values of a quasiparticle cutoff: 40 MeV, 60 MeV, and 6000 MeV (an infinite cutoff). The difference in the corresponding HFB energies, $\Delta E^{\rm HFB}_{\mathbf{q}} = E^{\rm HFB}_{\mathbf{q},\rm qps} - E^{\rm HFB}_{\mathbf{q},\rm can}$, is also shown.

3.1.2. PNP in canonical and quasiparticle bases

The particle number projection in the canonical basis had been incorporated to the HFBTHO program since its initial release. On the other hand, the new version of the program contains the particle number projection performed in the quasiparticle basis. The two PNP methods are distinct and can under certain circumstances yield different results. Most notably, a difference will arise if the underlying HFB calculations enforce a cutoff in the quasiparticle space. The introduction of such a cutoff is a common way to render the energies convergent for zero-range pairing interactions and is therefore an integral part of Skyrme-EDF calculations with HFBTHO [11].

To compare the two methods, Fig. 2 shows the difference between the PNP energies obtained in the quasiparticle and in the canonical basis, $\Delta E^{\rm PNP}_{\mathbf{q}} = E^{\rm PNP}_{\mathbf{q},\rm qps} - E^{\rm PNP}_{\mathbf{q},\rm can}$, for three different values of a quasiparticle cutoff. We consider a range of quadrupole deformations in ^{50}Cr, $\langle\hat{Q}_{20}\rangle \in [-2.0\text{ b}, 4.0\text{ b}]$, and keep the other parameters fixed. For a relatively low cutoff ($E_{\rm cut} = 40$ MeV), the difference is $\Delta E^{\rm PNP}_{\mathbf{q}} \leq 0.5$ MeV. For a cutoff value typically used in realistic calculations ($E_{\rm cut} = 60$ MeV), the difference reduces to $\Delta E^{\rm PNP}_{\mathbf{q}} \leq 0.2$ MeV. Finally, in the limit of an infinite cutoff ($E_{\rm cut} = 6000$ MeV) the difference between the two methods vanishes.

In addition, Fig. 2 shows the difference between the HFB energies obtained in the quasiparticle and in the canonical basis,

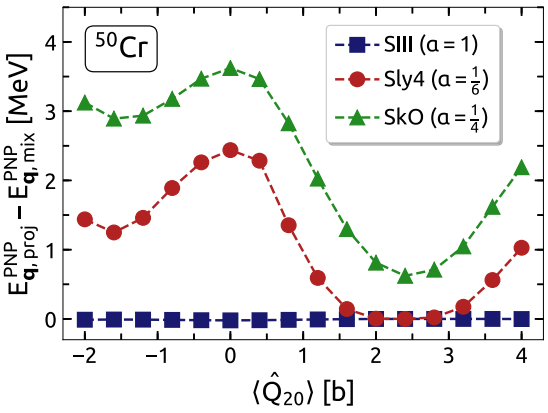

Fig. 3. The difference between the PNP energies obtained with the mixed and the projected density prescription. We consider three Skyrme EDFs whose volume terms depend on different powers of density α.

$\Delta E^{HFB}_{\mathbf{q}} = E^{HFB}_{\mathbf{q},qps} - E^{HFB}_{\mathbf{q},can}$, for the three cutoff values. The HFB curves largely follow the corresponding PNP curves, corroborating the fact that the discrepancy in projected energies stems from the initial difference in HFB states. Finally, an instructive limit to consider is the case of a collapsing pairing interaction, which is a common feature of PNP models that perform variation before projection [14]. Note that the collapse of pairing happens around $\langle\hat{Q}_{20}\rangle = 2.5$ b in our calculation. Regardless of the cutoff, the two PNP methods then yield the same energy that also coincides with the HFB energy.

3.1.3. The choice of density prescription

As discussed in Sec. 2.1.6, the new implementation of PNP enables the choice of density prescription for the parts of an EDF that depend on non-integer powers of density. In order to quantify the consequences of this choice, Fig. 3 shows the difference between the PNP energies obtained with the mixed and the projected density prescription. We consider three Skyrme EDFs whose volume terms depend on different powers of density α: SIII ($\alpha = 1$) [44], Sly4 ($\alpha = \frac{1}{6}$) [45], and SkO ($\alpha = \frac{1}{4}$) [46]. For all three EDFs, the Coulomb exchange term depends on the 4/3-th power of the proton density.

For SIII, the entire difference between the two prescriptions lies in the Coulomb exchange term. In ^{50}Cr, this difference amounts to about 0.1% of the term, or about 0.01 MeV, and is therefore not visible in Fig. 3. On the other hand, for Sly4 and SkO an additional difference in the volume term comes into play. The difference in this term amounts to about 0.1% as well, but it translates to a sizeable absolute difference of $2-3$ MeV. Again, the two prescriptions yield the same result in the limit of a collapsing pairing interaction (around $\langle\hat{Q}_{20}\rangle = 2.5$ b). We note that the difference from density prescriptions does *not* scale with nuclear mass and that it remains of comparable magnitude even in the heaviest nuclei.

Unfortunately, to the best of our knowledge, there are no published comparisons of PNP energies obtained with different density prescriptions. However, Ref. [47] contains the comparison between the PNP dynamic moments of inertia obtained with the mixed and the projected density prescription, using a Gogny EDF and the Lipkin-Nogami approximation. The reported difference is sizeable and generally of the order of a few percent.

3.1.4. Benchmarking against HFODD

To further verify our implementation, we tested the PNP results of HFBTHO against results obtained with HFODD. Since the latest release of the code [13] cannot project on both protons and neutrons and does not give a full breakdown of the projected energy, we use for our benchmark a recent, still unpublished, modification of the HFODD solver based on version 2.73 [6]. In this version, PNP is implemented in the canonical basis and the results must thus be tested against the original HFBTHO implementation [11]. As demonstrated in Section 3.1.2, this implementation of PNP (in the canonical basis) gives the same results as the new implementation (in the quasiparticle basis) for infinite cutoffs.

Table 1
The breakdown of the PNP energy (in MeV) of the $\langle\hat{Q}_{20}\rangle = 1$ b configuration in ^{50}Cr, obtained with the HFBTHO and HFODD solvers. A spherical HO basis with $N_0 = 12$ shells and the SIII EDF were used; see text for more details on the parameters of the calculation.

	HFBTHO	HFODD
$E^{(n)}_{kin}$	466.236124	466.236123
$E^{(p)}_{kin}$	415.937244	415.937243
$E^{\rho\rho}$	-1701.776220	-1701.776217
$E^{\rho\tau}$	201.410935	201.410934
$E^{\rho\Delta\rho}$	126.141959	126.141958
$E^{\rho\nabla J}$	-39.203075	-39.203075
$E^{(n)}_{pair}$	-0.333798	-0.333798
$E^{(p)}_{pair}$	-0.981203	-0.981203
E_{PNP}	-532.568034	-532.568034

Table 1 contains a breakdown of the PNP energy of the $\langle\hat{Q}_{20}\rangle = 1$ b configuration in ^{50}Cr, obtained with the HFBTHO and HFODD solvers. The calculation parameters are the same as those described at the beginning of this section, except that (i) $N_0 = 12$ HO shells are used, (ii) a surface-volume pairing interaction is used, and (iii) the Coulomb interaction is entirely neglected. In both HFBTHO and HFODD calculations, $N_\varphi = 15$ gauge angles were used for both neutrons and protons. The HFODD results correspond to a Gauss quadrature characterized by NXHERM = NYHERM = NZHERM = 30 points. The largest difference, for the density-dependent volume term, does not exceed 3 eV.

3.2. Angular momentum projection

Next, we perform the illustrative angular momentum projection calculations, using the same parameters as described at the beginning of Section 3.1.

3.2.1. Convergence of angular momentum decomposition

To start with, we test the convergence of AMP energies [$E^{AMP}_{\mathbf{q}} \equiv E^{J;p}_{\mathbf{q}}$, Eq. (14)] and decompose an HFB state onto different values of angular momenta [$|c^{J;p}_{\mathbf{q}}|^2$, Eq. (13)]. As before, the quadrupole moment of the reference HFB state is constrained to $\langle\hat{Q}_{20}\rangle = 1$ b, the dipole and the octupole moment are constrained to zero, while higher multipole moments are determined self-consistently. Fig. 4(a) shows the AMP energies for $J^p = 0^+, 2^+, 4^+$, and 6^+ as a function of the number of rotational angles N_β. Note that the considered configuration is reflection-symmetric and thus only positive-parity states can be obtained. In turn, the projection interval is reduced to $\beta \in [0, \pi/2]$. As expected, the convergence is faster for lower values of J. For all J, an excellent agreement with the fully converged solution (represented by the dashed horizontal lines and computed for $N_\beta = 100$) is obtained already for $N_\beta = 10$. The convergence pattern will generally depend on the properties of the HFB state (e.g., the magnitude of the quadrupole deformation or whether the parity is broken), as well as on the value of J. Consequently, in practical applications, one should verify the convergence of AMP with respect to N_β.

Furthermore, Fig. 4(b) shows the decomposition of the same HFB state onto different values of angular momentum. The maxi-

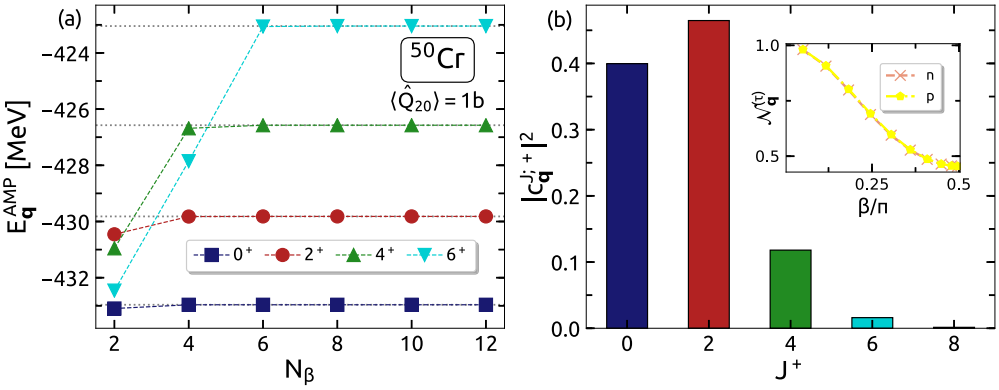

Fig. 4. Angular momentum projection in the spherical HO basis for the $\langle\hat{Q}_{20}\rangle = 1$ b configuration in ^{50}Cr. (a): The AMP energy of the $J^p = 0^+, 2^+, 4^+$, and 6^+ state as a function of the number of rotational angles N_β. The dashed horizontal line denotes the fully converged solution ($N_\beta = 100$). (b): The decomposition of an HFB state onto different angular momenta for $N_\beta = 10$. The inset shows the corresponding overlaps for neutrons and protons.

mum is found for $J = 2$, $|c^{J;+}_{\mathbf{q}}|^2 = 0.4649$, while the coefficients for $J \geq 8$ components are negligible. The inset shows the corresponding overlaps for both neutrons and protons [$\mathcal{N}^{(\tau)}_{\boldsymbol{q}}(\beta, 0)$, Eq. (15)]. The overlaps for the two types of particles are very similar: they are real and monotonously decrease from $\mathcal{N}^{(\tau)}_{\boldsymbol{q}}(0, 0) = 1$ to their respective minimal values at $\beta = \pi/2$. Since the quadrupole deformation is rather moderate, the overlaps at $\beta = \pi/2$ are still sizeable. Note that the overlaps for $\beta \in [\pi/2, \pi]$ can be obtained by a reflection around the $\beta = \pi/2$ vertical axis; see Section 2.1.4.

3.2.2. Benchmarking against HFODD

In full analogy with the case of PNP discussed in Section 3.1.4, we can benchmark the AMP results obtained with HFBTHO against the results obtained with HFODD. The main restriction in this case is that HFODD requires the usage of a spherical HO basis. Once again, we consider the $\langle\hat{Q}_{20}\rangle$=1 b configuration in ^{50}Cr. The calculation parameters are the same as those described at the beginning of Section 3.1, except that (i) the Coulomb interaction is entirely neglected, (ii) all the higher multipole moments up to the eighth order are constrained to zero, and (iii) in order to additionally probe the contribution from the tensor term of the functional, we used the SLy5 parametrization of the Skyrme EDF [45]. In this case, the parameterizations of the pairing interaction yields pairing gaps that are much smaller than the experimental ones. However, since our goal is simply to compare the two codes against one another, this discrepancy is irrelevant. All the AMP calculations were performed with $N_\beta = 30$ rotational angles $\beta \in [0, \pi]$.

We compared our results to those generated with the latest release of HFODD, where the AMP is implemented in the Hartree-Fock basis [13]. Because the two codes employ different bases, the obtained HFB energies slightly differ and agree within 2.2 keV. For the projected energies, the difference does not exceed 12 keV for the range of angular momentum $J \in [0, 10]$. Although this test is already very encouraging, we can go one step further and test separately each contribution to the projected energy. To this end, we use the same unpublished version of HFODD built on top of the version 2.73 that was employed for the PNP benchmark. In that version of the code, the AMP is implemented in the HO basis so a closer comparison is possible. As expected, we find that the HFB energies agree within 1 eV: $E_{\text{HFB}} = -531.370615$ MeV.

Table 2 contains the breakdown of the AMP energy for angular momentum $J = 0$ and $J = 8$; see Eqs. (54) - (55) for the definition of each term. For the $J = 0$ state, the differences between the two codes do not exceed 10 eV, with most terms agreeing within 2 eV. Not surprisingly, the differences increase a little for the $J = 8$ case. However, they are still of the order of a few dozens or hundreds of eV, and overall less than 1 keV. Considering the remaining differences between the two codes – HFODD works with the Cartesian basis and implements the full 3D rotation of wave functions while HFBTHO works with the cylindrical basis and implements only the rotation in the Euler angle β – this benchmark is quite conclusive.

3.2.3. AMP in a deformed basis

One of the main advantages of the present implementation of AMP is that it can be performed in bases that are not closed under rotation. Such deformed (or stretched) bases are often used in calculations of potential energy surfaces because they provide a computationally efficient way to obtain precise representations of arbitrarily deformed HFB configurations. The main downside of using a deformed basis is the need to carefully study the convergence of calculations as a function of the basis deformation; see [48] for a discussion of the impact of basis truncation on HFB observables. In this section, we demonstrate that the convergence pattern of AMP calculations is generally different from the one of the underlying HFB calculations.

Fig. 5 shows the HFB energy and the AMP ($J^p = 0^+$) energy in ^{50}Cr as a function of the axial quadrupole moment $\langle\hat{Q}_{20}\rangle$ and obtained with three different HO bases: the spherical (β_2=0.0) basis, the prolate-deformed ($\beta_2 = 0.1$) basis, and the oblate-deformed (β_2=−0.1) basis. N_0=8 HO shells were used in all three cases. For configurations with moderate prolate deformation, the 0^+ energies obey $E_{J=0}(\beta_2 = -0.1) < E_{J=0}(\beta_2 = 0.0) < E_{J=0}(\beta_2 = 0.1)$. The differences in HFB energies are much smaller, but they obey the exact opposite rule: $E_{\text{HFB}}(\beta_2 = -0.1) > E_{\text{HFB}}(\beta_2 = 0.0) > E_{\text{HFB}}(\beta_2 = 0.1)$. Interestingly, the pattern is reversed for configurations with moderate oblate deformation. For them, the prolate-deformed basis gives the lowest 0^+ energy and the oblate-deformed basis gives the highest 0^+ energy. In addition, the pattern is further modified as the deformation increases: for configurations with $\langle\hat{Q}_{20}\rangle \gtrapprox 5.4$ b the HFB and the 0^+ energy follow the same ordering and the lowest energies are obtained with the prolate-deformed basis.

The observed difference in patterns may have two main origins:

- **Numerical Precision.** For a prolate-deformed basis, the number of basis states along the z-axis of the reference frame, which coincides with the elongation axis of the HFB configuration, is larger than the number of states along the perpendicular axis. Consequently, the prolate-deformed HFB configuration is numerically well described. However, the elongation axis of the rotated HFB configuration is not anymore aligned with the z-axis of the reference frame. In fact, for $\beta = \pi/2$ it is aligned with the axis perpendicular to it – where the number of basis states is lower. Rotated prolate-deformed configurations are thus described less precisely in a prolate-deformed basis. Moreover, the weight of each rotated configuration is

Table 2
The breakdown of the AMP energy (in MeV) of the $\langle \hat{Q}_{20} \rangle = 1$ b configuration in ^{50}Cr, obtained with the HFBTHO and HFODD solvers. Energies for $J = 0$ (top) and $J = 8$ (bottom) are shown. A spherical HO basis with $N_0 = 8$ shells and the Sly5 EDF were used; see text for more details on the parameters of the calculation.

$J = 0$	HFBTHO	HFODD
$E^{(n)}_{\text{kin}}$	475.811944	475.811932
$E^{(p)}_{\text{kin}}$	418.693797	418.693807
$E^{\rho\rho}$	-1797.938577	-1797.938577
$E^{\rho\tau}$	269.775424	269.775424
$E^{\rho\Delta\rho}$	149.166859	149.166858
$E^{\rho\nabla J}$	-42.039341	-42.039339
E^{JJ}	1.213084	1.213084
E^{ss}	0.251440	0.251439
E^{sj}	0.287586	0.287585
$E^{s\Delta s}$	0.111281	0.111280
$E^{s\nabla J}$	0.137866	0.137865
E^{sT}	0.009186	0.009186
$E^{(n)}_{\text{pair}}$	-2.848138	-2.848137
$E^{(p)}_{\text{pair}}$	-4.507887	-4.507885
E_{AMP}	-532.307952	-532.307950

$J = 8$	HFBTHO	HFODD
$E^{(n)}_{\text{kin}}$	467.384564	467.384572
$E^{(p)}_{\text{kin}}$	437.860544	437.860226
$E^{\rho\rho}$	-1812.483313	-1812.482960
$E^{\rho\tau}$	275.246980	275.246855
$E^{\rho\Delta\rho}$	148.724958	148.724962
$E^{\rho\nabla J}$	-40.088099	-40.088112
E^{JJ}	0.997760	0.997763
E^{ss}	-1.279415	-1.279386
E^{sj}	-1.763059	-1.763017
$E^{s\Delta s}$	-0.559418	-0.559406
$E^{s\nabla J}$	-0.449841	-0.449832
E^{sT}	-0.070601	-0.070600
$E^{(n)}_{\text{pair}}$	-1.159525	-1.159544
$E^{(p)}_{\text{pair}}$	-2.563745	-2.563772
E_{AMP}	-527.963805	-527.963895

$\sin\beta\, d^J_{00}(\beta)$. For $J = 0$, $d^0_{00}(\beta) = 1$, and the weight is simply $\sin\beta$. Consequently, the $\beta \approx \pi/2$ configurations, which are numerically less precise, have larger weights than the $\beta \approx 0$ configurations, which are numerically more precise. For $J > 0$, the function $\sin\beta\, d^J_{00}(\beta)$ is not monotonous and this simple analysis does not hold anymore.

- **The Effect of the Rotation Matrix.** The rotation matrix [Eq. (24)] enters the calculation of overlaps [Eq. (15)]. Furthermore, the overlaps enter the calculation of the norm overlap kernel $\mathcal{N}^{J;p}_{\boldsymbol{q}}$ and the Hamiltonian kernel $\mathcal{H}^{J;p}_{\boldsymbol{q}}$, both of which are needed to calculate the AMP energy [Eq. (14)]. However, the properties of the rotation matrix depend on the basis deformation. For example, the determinant of the rotation matrix equals to 1 in the spherical basis and decreases rapidly as the basis deformation increases. Without actually performing the calculations, it is not clear how the deformation *of the basis* impacts the rotation matrix, the subsequent kernels and, eventually, the AMP energy.

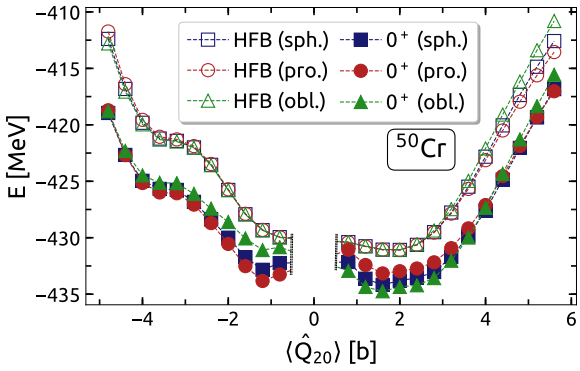

Fig. 5. Total HFB and $J^p = 0^+$ energy of ^{50}Cr as a function of the constraint on the axial quadrupole moment $\langle \hat{Q}_{20} \rangle$. Blue curves with squares show results obtained with a spherical basis; red curves with circles show results obtained with a prolate-deformed basis of $\beta_2 = 0.1$; green curves with triangles show results obtained with an oblate-deformed basis of $\beta_2 = -0.1$. Plain symbols correspond to AMP results and open symbols to HFB ones; see text for additional details.

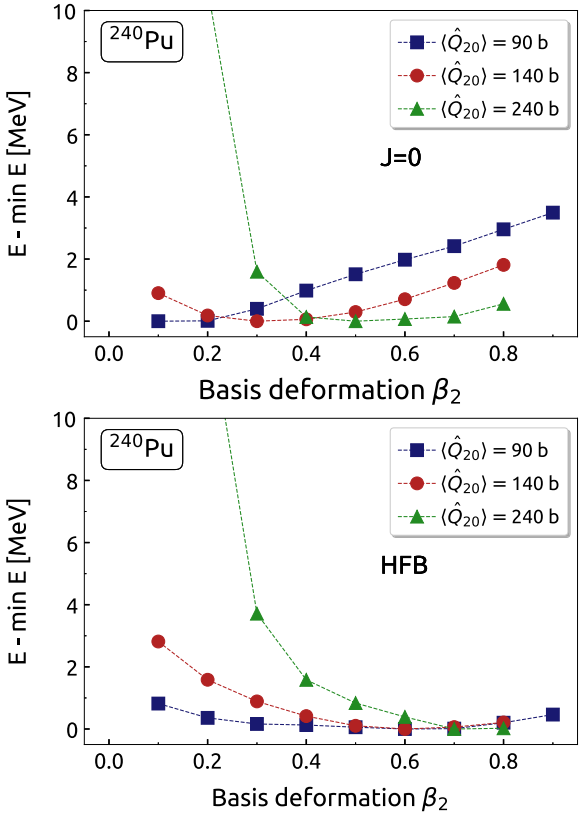

Fig. 6. The convergence of the HFB energy (bottom) and the AMP 0^+ energy (top) as a function of the basis deformation β_2 for three configurations along the fission path of ^{240}Pu: $(Q_{20}, Q_{30}) = (90\,\text{b}, 0\,\text{b}^{3/2})$, $(Q_{20}, Q_{30}) = (140\,\text{b}, 12\,\text{b}^{3/2})$, and $(Q_{20}, Q_{30}) = (240\,\text{b}, 25\,\text{b}^{3/2})$. All curves are normalized relative to their respective minima over the interval $\beta_2 \in [0, 0.9]$; see text for additional details.

To get a better idea of the convergence pattern of AMP calculations as a function of the basis deformation, Fig. 6 shows a semi-realistic example of the fission path of ^{240}Pu. We considered three different configurations along the path: $(Q_{20}, Q_{30}) = (90\,\text{b}, 0\,\text{b}^{3/2})$, $(Q_{20}, Q_{30}) = (140\,\text{b}, 12\,\text{b}^{3/2})$, and $(Q_{20}, Q_{30}) = (240\,\text{b}, 25\,\text{b}^{3/2})$. For each configuration, we computed the HFB solution in a basis characterized by $N_0^{\max} = 24$ HO shells and $\beta_2 = 0.0, 0.1, \ldots, 0.9$ deformation. In addition, the basis was truncated and only the low-

est $N_{\text{states}} = 1100$ states were retained. The spherical-equivalent oscillator length b_0 was *not* adjusted and was instead fixed at $b_0 = 2.288$ fm. In other words, the oscillator lengths b_z and $b_\perp$ vary as a function of β_2 in such a way that the product $b_z b_\perp^2 = b_0^3$ is constant.

The HFB convergence pattern (bottom panel) should be familiar to the practitioners: very deformed configurations require (very) deformed bases. In our example, the lowest HFB energy is found for $\beta_2 = 0.6$ ($\langle \hat{Q}_{20} \rangle = 90$ b and $\langle \hat{Q}_{20} \rangle = 140$ b) and for $\beta_2 = 0.8$ ($\langle \hat{Q}_{20} \rangle = 240$ b). Note that, in principle, one should also adjust the oscillator frequency as a function of the deformation; see discussion in [48]. For very deformed configurations, the convergence pattern of the 0^+ energy is qualitatively similar to the HFB pattern in the sense that the minimum is obtained for non-zero β_2 values. However, these values are significantly smaller than in the HFB case. In fact, for the least-deformed configuration (which approximately corresponds to the fission isomer), the lowest 0^+ energy is obtained for a spherical basis. These results suggest that large-scale applications of AMP in a deformed basis should be accompanied by a careful study of the numerical convergence.

3.2.4. Limitations of the model

The user should be aware of a number of limitations of the novel symmetry restoration module, related to both the underlying physics and the numerical implementation:

- **Projection of the Eigenstates.** Some HFB configurations are already eigenstates of an operator related to the symmetry being restored. For example, the spherical configuration is an eigenstate of the angular momentum operator with the eigenvalue $J = 0$. Similarly, configurations with vanishing odd multipole moments are eigenstates of the parity operator with the eigenvalue $p = +1$. Projecting these configurations onto other eigenvalues ($J = 1, 2, \ldots$ for the former and $p = -1$ for the latter) will yield non-physical results. In practice, one should be cautious because numerical issues can occur already for configurations that are sufficiently close to being eigenstates.
- **Invertibility of the Rotation Matrix.** The inverse and the determinant of the rotation matrix enter our calculations explicitly. However, as the size and the deformation of the basis increase, the determinant drops rapidly and the matrix can become numerically non-invertible for some rotational angles close to $\beta = \pi/2$. These angles are then disregarded in AMP, under the assumption that the corresponding overlaps are negligible. This assumption is justified for very deformed configurations, but it can break down for configurations with moderate or small deformations. Consequently, caution is advised when calculating moderately deformed configurations with deformed bases. In particular, the description of near-spherical configurations with deformed bases is imprecise and should therefore be avoided.
- **Spuriosity of Projected Energies.** The Hamiltonian kernel is formally not well-defined for EDFs that are density-dependent or omit parts of the interaction. In the worst case scenario, this can lead to sizeable finite steps and even divergences in projected energies. Such spuriosities were abundantly reported in PNP [49–52], while AMP in even-even nuclei seems to remain issue-free [22]. In many practical implementations, however, the scale of these spuriosities is smaller than the errors due to the various numerical limitations. Nevertheless, as the quest for spuriosity-free EDFs is under way, the user should remain aware of this formal limitation.

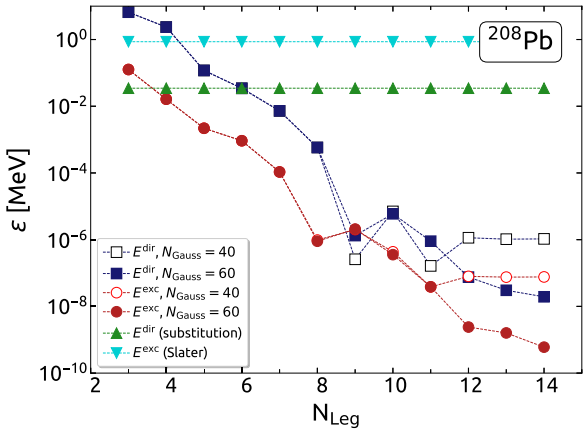

Fig. 7. The absolute error (in MeV) of the Gaussian expansion of the Coulomb potential as a function of Gauss-Legendre quadrature points, i.e., the number of Gaussians approximating $1/r$; see Eq. (62).

3.3. Exact Coulomb

We tested our implementation of the "exact" Coulomb calculation by comparing results obtained with the new version of HFBTHO and with the Gogny code used in [53,54]. In the latter, all contributions of the Coulomb interaction (direct, exchange, and pairing) are computed exactly thanks to the properties of the spherical HO basis.

For numerical comparison, we consider the ^{208}Pb nucleus and use the D1S Gogny EDF. Furthermore, we disregard the two-body center-of-mass correction and neglect the Coulomb contribution to pairing. Calculations are performed in a spherical HO basis with $N_0 = 12$ shells and the oscillator length $b_0 = 2.5$ fm. They were converged up to 10^{-12}. Fig. 7 shows the absolute error $\varepsilon = |E^X_{\text{HFBTHO}} - E^X_{\text{Gogny}}|$ as a function of the number of Gauss-Legendre quadrature points N_{Leg}. Here, X stands for either the direct or the exchange contribution to the Coulomb energy, and the subscripts "HFBTHO" and "Gogny" refer to the HFBTHO 4.0 and the spherical Gogny code, respectively.

For $N_{\text{Gauss}} = 60$ points in both the Gauss-Hermite and Gauss-Laguerre integrations (the full lines), the expansion of the Coulomb potential onto Gaussians converges nicely to the exact value. In particular, at $N_{\text{Leg}} = 14$, the difference is 20 meV and 1 meV for the direct and the exchange term, respectively. If the number of quadrature points is reduced to $N_{\text{Gauss}} = 40$ (the dashed lines), we observe a saturation of convergence at about 1 eV (direct) and 80 meV (exchange) at $N_{\text{Leg}} = 14$. For comparison, we also show the results of the "standard" prescription for the direct term, which is based on the substitution method in a box of size $L = 50$ fm with 80 Gauss-Legendre quadrature points; see discussion in [12], and for the exchange term, which is computed at the Slater approximation.

4. Input data file

The input data file format remains similar to version 3.00 and only contains one additional namelist.

4.1. Sample input file

```
&HFBTHO_GENERAL
 number_of_shells = 10,
 oscillator_length = -1.0,
 basis_deformation = 0.0,
 proton_number = 24, neutron_number = 26,
 type_of_calculation = 1 /
```

```
 &HFBTHO_INITIAL
 beta2_deformation = 0.0,
 beta3_deformation = 0.0,
 beta4_deformation = 0.0 /
&HFBTHO_ITERATIONS
 number_iterations = 100, accuracy = 1.E-5,
 restart_file = -1 /
&HFBTHO_FUNCTIONAL
 functional = 'SLY4',
 add_initial_pairing = F,
 type_of_coulomb = 2 /
&HFBTHO_PAIRING
 user_pairing = F,
 vpair_n = -300.0, vpair_p = -300.0,
 pairing_cutoff = 60.0,
 pairing_feature = 0.5 /
&HFBTHO_CONSTRAINTS
 lambda_values = 1, 2, 3, 4, 5, 6, 7, 8,
 lambda_active = 0, 0, 0, 0, 0, 0, 0, 0,
 expectation_values = 0.0, 0.0, 0.0, 0.0,
 0.0, 0.0, 0.0, 0.0 /
&HFBTHO_BLOCKING
 proton_blocking = 0, 0, 0, 0, 0,
 neutron_blocking = 0, 0, 0, 0, 0 /
&HFBTHO_PROJECTION
 switch_to_THO = 0,
 projection_is_on = 0, gauge_points = 1,
 delta_Z = 0, delta_N = 0 /
&HFBTHO_TEMPERATURE
 set_temperature = F, temperature = 0.0 /
&HFBTHO_FEATURES
 collective_inertia = F,
 fission_fragments = F,
 pairing_regularization = F,
 localization_functions = F /
&HFBTHO_NECK
 set_neck_constrain = F, neck_value = 0.5 /
&HFBTHO_DEBUG
 number_Gauss = 40, number_Laguerre = 40,
 number_Legendre = 80,
 compatibility_HFODD = F,
 number_states = 500,
 force_parity = T, print_time = 0 /
&HFBTHO_RESTORATION
 PNP_is_on = 0, number_of_gauge_points = 1,
 delta_neutrons = 0, delta_protons = 0,
 AMP_is_on = 0,
 number_of_rotational_angles = 1,
 maximal_angular_momentum = 0 /
```

4.2. Description of input data

We now define the new or updated inputs introduced in version 4.0.

Keyword: `HFBTHO_FUNCTIONAL`

• `type_of_coulomb = 2`: Logical switch that defines the treatment of the Coulomb potential. In previous versions, this switch could only take values 0 (no Coulomb), 1 (direct contribution only) or 2 (direct and exchange contribution with the Slater approximation). In the current version, the following new options are also available:

-1: direct Coulomb only by sum of N_c Gaussians;
-2: direct Coulomb by the substitution method, exchange Coulomb by sum of N_c Gaussians;
-3: direct Coulomb by sum of N_c Gaussians, exchange Coulomb with the Slater approximation;
-4: direct and exchange Coulomb by sum of N_c Gaussians;
-5: direct, exchange, and pairing Coulomb by sum of N_c Gaussians.

Here, N_c is the number of Gaussians in (62). It is stored in the UNEDF module variable `n_g_coul` and is preset at `n_g_coul=9` in the file `hfbtho_unedf.f90`. There is no option to change this number directly in the input file. Default: 2.

Keyword: `HFBTHO_RESTORATION`

• `PNP_is_on = 0`: Logical switch that activates the particle number projection in the quasiparticle basis. When set to 1 the mixed density prescription is used and when set to 2 the projected density prescription is used (see Sections 2.1.6 and 3.1.3). This option is different from the old `projection_is_on` switch in the `HFBTHO_PROJECTION` namelist, which activates PNP with the mixed density prescription in the canonical basis. For an infinite quasiparticle cutoff, the two mixed density prescription options should give the same result. This option is incompatible with: finite-temperature, THO basis, and blocking calculations. Default: 0;

• `number_of_gauge_points = 1`: Number of gauge angles N_φ for particle number projection. The same number N_φ is used for protons and neutrons. Default: 1;

• `delta_neutrons = 0`: Value of the shift in neutron number δN. In the case of PNP, one can project on all even neutron numbers in the interval $[N_0 - \delta N, N_0 + \delta N]$, where N_0 is the number of neutrons of the considered nucleus (even only for PNP). Default: 0;

• `delta_protons = 0`: Value of the shift in proton number δZ. In the case of PNP, one can project on all even proton numbers in the interval $[Z_0 - \delta Z, Z_0 + \delta Z]$, where Z_0 is the number of protons of the considered nucleus (even only for PNP). Default: 0;

• `AMP_is_on = 0`: Logical switch that activates (if equal to 1) the restoration of angular momentum J and parity p. This option can be combined with PNP to carry out a simultaneous projection on N, Z, J, and p. It is incompatible with: finite-temperature, THO basis, and blocking calculations. Default: 0;

• `number_of_rotational_angles = 1`: Number of rotational angles N_β use for AMP. Internally, the code will readjust N_β if reflection symmetry is enforced. In such a case, the program will compute either $N_\beta/2$ (N_β even) or $(N_\beta + 1)/2$ (N_β odd) rotational angles (see Section 2.1.4). Default: 1;

• `maximal_angular_momentum = 0`: Maximum value of the angular momentum $J_{\max}$. In the case of AMP, all even values of J in $[0, J_{\max}]$ (parity conserved) or all values J in $[0, J_{\max}]$. Default: 0.

5. Program HFBTHO

5.1. Structure of the code

Compared with version 3.00, we have substantially increased the modularization of the source code since the number of modules increased from 18 to 25. The code is organized as follows:

- `hfbtho_bessel.f90`: defines the modified Bessel functions of order 0 and 1;
- `hfbtho_canonical.f90`: defines the canonical basis of the HFB theory;

- `hfbtho_collective.f90`: computes the ATDHF and GCM collective inertia tensor and zero-point energy correction in the perturbative cranking approximation; see [5] and references therein;
- `hfbtho_elliptic_integrals.f90`: defines complete elliptic integral of the second kind used for the Coulomb potential;
- `hfbtho_fission.f90`: computes the charge, mass, and axial multipole moments of fission fragments and the value of the Gaussian neck operator;
- `hfbtho_gauss.f90`: defines the quadrature meshes: Gauss-Hermite, Gauss-Laguerre, and Gauss-Legendre;
- `hfbtho_gogny.f90`: computes the matrix elements of the Gogny force as well as the corresponding mean field and pairing field;
- `hfbtho_io.f90`: contains a collection of routines handling inputs and outputs;
- `hfbtho_large_scale.f90`: contains a collection of routines for mass table, drip lines, or potential energy surface calculations, as well as for the parallelization of single HFB calculations;
- `hfbtho_library.f90`: provides the definition of the main routine `Main_Program()` that launches complete HFBTHO calculations: stand-alone, mass tables, drip lines, or potential energy surfaces;
- `hfbtho_lipkin.f90`: calculates the Lipkin-Nogami correction, including the λ_2 parameters, densities, and energies;
- `hfbtho_localization.f90`: computes spatial localization functions;
- `hfbtho_main.f90`: calls the `Main_Program()` routine;
- `hfbtho_math.f90`: contains a collection of general-use mathematical routines;
- `hfbtho_multipole_moments.f90`: computes the expectation value and matrix elements of axial multipole moments;
- `hfbtho_pnp.f90`: implements particle number projection in the canonical basis;
- `hfbtho_projections.f90`: implements the angular momentum, particle number, and parity projection in the quasiparticle basis;
- `hfbtho_read_functional.f90`: contains a collection of routines to read the parameters of the EDF from a file;
- `hfbtho_solver.f90`: solves the self-consistent iterations of the HFB theory;
- `hfbtho_storage.f90`: contains an interface to the QRPA pnFAM code; see [55] and references therein;
- `hfbtho_tho.f90`: defines the transformed harmonic oscillator basis; see [11] and references therein;
- `hfbtho_unedf.f90`: defines parameterizations of the Skyrme and Gogny functionals, and computes density-dependent coupling constants and fields of generalized Skyrme energy functionals;
- `hfbtho_utilities.f90`: defines the integer and real types used throughout the code, as well as various numerical constants;
- `hfbtho_variables.f90`: contains list of global variables used throughout the code;
- `hfbtho_version.f90`: version number (currently git commit number of the previous commit) and history of previous versions.

The programming language of most of the code is now Fortran 2003. The code HFBTHO requires an implementation of the BLAS and LAPACK libraries to function correctly. Shared memory parallelism is available via OpenMP pragmas.

This version comes with a built-in Doxygen documentation. To benefit from this feature, the user should install the doxygen software available at www.doxygen.org. The documentation is built by typing

```
make doc
```

By default, Doxygen generates only an on-line HTML documentation. The main page is located in the source directory at `./src/doc/html/index.html`. A PDF documentation can also be generated by going into `./doc/latex` and typing

```
make
```

The PDF file is named `refman.pdf`.

5.2. Running the code

The program ships with a Makefile that is preset for a number of Fortran compilers. The user should choose the compiler and set the path for the BLAS and LAPACK libraries. In version 4.0 of the code, we have simplified the call sequence of HFBTHO. Assuming an executable named `hfbtho_main` and a Linux system, execution is started by typing

```
./hfbtho_main [input_file_name]
```

where `[input_file_name]` is an optional name of the HFBTHO input file that contains all the Namelists. If none is given, the code will attempt to read the file with the generic name `hfbtho_NAMELIST.dat` in the current directory. The code will also automatically generate two ASCII output files: a compact one called `hfbtho.out` and a more extended one called `thoout.dat`. Finally, the code generates a binary file named `hfbtho_output.hel` that is used to restart calculations.

HFB calculations are greatly accelerated when OpenMP multithreading is activated. However, the user should keep in mind that this requires setting additional environment variables. In Linux/Unix machines, the default stack size is not large enough to run the code and must be increased. This can be achieved by instructions such as

```
ulimit -s unlimited
export OMP_STACKSIZE=32M
```

The value of `ulimit` defines the amount of stack size for the main OpenMP thread. OpenMP supports control over the stack size limit of all additional threads via the environment variable `OMP_STACKSIZE`. The value given above should be sufficient for all applications. Note that this value does not affect the stack size of the main thread set by `ulimit`. For completeness, note that the GNU OpenMP run-time (`libgomp`) recognizes the non-standard environment variable `GOMP_STACKSIZE`. If set, it overrides the value of `OMP_STACKSIZE`. Finally, the Intel OpenMP run-time library also recognizes the non-standard environment variable `KMP_STACKSIZE`. If set, it overrides the value of both `OMP_STACKSIZE` and `GOMP_STACKSIZE`.

Declaration of competing interest

The authors declare that they have no known competing financial interests or personal relationships that could have appeared to influence the work reported in this paper.

Acknowledgements

Support for this work was partly provided through Scientific Discovery through Advanced Computing (SciDAC) program funded by U.S. Department of Energy, Office of Science, Advanced Scientific Computing Research and Nuclear Physics. It was partly performed under the auspices of the US Department of Energy by the Lawrence Livermore National Laboratory under Contract DE-AC52-07NA27344 (code release number: LLNL-CODE-826901, document release number: LLNL-JRNL-827553). This work has been supported in part by the QuantiXLie Centre of Excellence, a project co-financed by the Croatian Government and European Union through the European Regional Development Fund - The Competitiveness and Cohesion Operational Programme (KK.01.1.1.01.0004). Computing support for this work came from the Lawrence Livermore National Laboratory (LLNL) Institutional Computing Grand Challenge program.

Appendix A. Densities and currents in the coordinate-space representation

Taking into account the block structure of the density matrix in the y-simplex basis [cf. Eq. (30)], we can write

$$\rho^{(\tau)}(\boldsymbol{r}\sigma,\boldsymbol{r}'\sigma') = \sum_{\alpha\gamma}\rho^{(\tau)++}_{\alpha\gamma}\Phi^{s=+i*}_{\gamma}(\boldsymbol{r}'\sigma')\Phi^{s=+i}_{\alpha}(\boldsymbol{r}\sigma) + \sum_{\alpha\gamma}\rho^{(\tau)--}_{\alpha\gamma}\Phi^{s=-i*}_{\gamma}(\boldsymbol{r}'\sigma')\Phi^{s=-i}_{\alpha}(\boldsymbol{r}\sigma), \tag{A.1}$$

where the sums run over HO basis states α and γ, while $\Phi^{s=+i}_{\gamma}(\boldsymbol{r}\sigma)$ and $\Phi^{s=-i}_{\gamma}(\boldsymbol{r}\sigma)$ are the coordinate space representations of the eigenstates of the y-simplex operator [cf. Eqs. (19) and (20)]

$$\Phi^{s=+i}_{\gamma}(\boldsymbol{r}\sigma) = \frac{1}{\sqrt{4\pi}}\psi_{n^{\alpha}_{z}}(z)\psi^{|\Lambda^{\alpha}|}_{n^{\alpha}_{\perp}}(r_{\perp}) \times\Big[ie^{i\Lambda^{\alpha}\phi}\chi_{+\frac{1}{2}}(\sigma)+e^{-i\Lambda^{\alpha}\phi}\chi_{-\frac{1}{2}}(\sigma)\Big], \tag{A.2a}$$

$$\Phi^{s=-i}_{\gamma}(\boldsymbol{r}\sigma) = \frac{1}{\sqrt{4\pi}}\psi_{n^{\alpha}_{z}}(z)\psi^{|\Lambda^{\alpha}|}_{n^{\alpha}_{\perp}}(r_{\perp}) \times\Big[e^{i\Lambda^{\alpha}\phi}\chi_{+\frac{1}{2}}(\sigma)+ie^{-i\Lambda^{\alpha}\phi}\chi_{-\frac{1}{2}}(\sigma)\Big]. \tag{A.2b}$$

Components of the HO eigenfunctions $\psi_{n^{\alpha}_{z}}(z)$ and $\psi^{|\Lambda^{\alpha}|}_{n^{\alpha}_{\perp}}(r_{\perp})$ are defined in [11] and $\chi_{\pm\frac{1}{2}}(\sigma)$ are the eigenstates of the z-component of the spin operator. Note that in Eq. (A.1) the dependence on $\boldsymbol{x}^{(\tau)}$ and $\boldsymbol{q}$ was dropped for compactness in both $\rho^{(\tau)}_{\boldsymbol{q}}(\boldsymbol{r}\sigma,\boldsymbol{r}'\sigma';\boldsymbol{x}^{(\tau)})$ on the left and $\rho^{(\tau)++}_{\boldsymbol{q},\alpha\gamma}(\boldsymbol{x}^{(\tau)})$, $\rho^{(\tau)--}_{\boldsymbol{q},\alpha\gamma}(\boldsymbol{x}^{(\tau)})$ on the right.

The auxiliary local densities (40a)-(40f) can then be calculated from Eq. (A.1) as

$$\rho^{(\tau)}(\boldsymbol{r}) = \sum_{\alpha\gamma}\rho^{(\tau)}_{\alpha\gamma,+}\mathcal{F}^{1}_{\alpha\gamma}(r_{\perp},z)\cos\Big[(\Lambda^{\alpha}-\Lambda^{\beta})\phi\Big], \tag{A.3a}$$

$$s^{(\tau)}_{r_{\perp}}(\boldsymbol{r}) = -\sum_{\alpha\gamma}\rho^{(\tau)}_{\alpha\gamma,-}\mathcal{F}^{1}_{\alpha\gamma}(r_{\perp},z)\sin\Big[(\Lambda^{\alpha}+\Lambda^{\beta}+1)\phi\Big], \tag{A.3b}$$

$$s^{(\tau)}_{\phi}(\boldsymbol{r}) = -\sum_{\alpha\gamma}\rho^{(\tau)}_{\alpha\gamma,-}\mathcal{F}^{1}_{\alpha\gamma}(r_{\perp},z)\cos\Big[(\Lambda^{\alpha}+\Lambda^{\beta}+1)\phi\Big], \tag{A.3c}$$

$$s^{(\tau)}_{z}(\boldsymbol{r}) = i\sum_{\alpha\gamma}\rho^{(\tau)}_{\alpha\gamma,+}\mathcal{F}^{1}_{\alpha\gamma}(r_{\perp},z)\sin\Big[(\Lambda^{\alpha}-\Lambda^{\beta})\phi\Big], \tag{A.3d}$$

$$\tau^{(\tau)}(\boldsymbol{r}) = \sum_{\alpha\gamma}\rho^{(\tau)}_{\alpha\gamma,+}\mathcal{F}^{2}_{\alpha\gamma}(r_{\perp},z)\cos\Big[(\Lambda^{\alpha}-\Lambda^{\beta})\phi\Big], \tag{A.3e}$$

$$T^{(\tau)}_{r_{\perp}}(\boldsymbol{r}) = -\sum_{\alpha\gamma}\rho^{(\tau)}_{\alpha\gamma,-}\mathcal{F}^{3}_{\alpha\gamma}(r_{\perp},z)\sin\Big[(\Lambda^{\alpha}+\Lambda^{\beta}+1)\phi\Big], \tag{A.3f}$$

$$T^{(\tau)}_{\phi}(\boldsymbol{r}) = -\sum_{\alpha\gamma}\rho^{(\tau)}_{\alpha\gamma,-}\mathcal{F}^{3}_{\alpha\gamma}(r_{\perp},z)\cos\Big[(\Lambda^{\alpha}+\Lambda^{\beta}+1)\phi\Big], \tag{A.3g}$$

$$T^{(\tau)}_{z}(\boldsymbol{r}) = i\sum_{\alpha\gamma}\rho^{(\tau)}_{\alpha\gamma,+}\mathcal{F}^{2}_{\alpha\gamma}(r_{\perp},z)\sin\Big[(\Lambda^{\alpha}-\Lambda^{\beta})\phi\Big], \tag{A.3h}$$

$$j^{(\tau)}_{r_{\perp}}(\boldsymbol{r}) = \frac{1}{2i}\sum_{\alpha\gamma}\rho^{(\tau)}_{\alpha\gamma,+}\mathcal{F}^{4}_{\alpha\gamma}(r_{\perp},z)\cos\Big[(\Lambda^{\alpha}-\Lambda^{\beta})\phi\Big], \tag{A.3i}$$

$$j^{(\tau)}_{\phi}(\boldsymbol{r}) = \frac{1}{2i}\sum_{\alpha\gamma}\rho^{(\tau)}_{\alpha\gamma,+}\mathcal{F}^{5}_{\alpha\gamma}(r_{\perp},z)\sin\Big[(\Lambda^{\beta}-\Lambda^{\alpha})\phi\Big], \tag{A.3j}$$

$$j^{(\tau)}_{z}(\boldsymbol{r}) = \frac{1}{2i}\sum_{\alpha\gamma}\rho^{(\tau)}_{\alpha\gamma,+}\mathcal{F}^{6}_{\alpha\gamma}(r_{\perp},z)\cos\Big[(\Lambda^{\alpha}-\Lambda^{\beta})\phi\Big], \tag{A.3k}$$

$$J^{(\tau)}_{r_{\perp}r_{\perp}}(\boldsymbol{r}) = i\sum_{\alpha\gamma}\rho^{(\tau)}_{\alpha\gamma,-}\mathcal{F}^{4}_{\alpha\gamma}(r_{\perp},z)\sin\Big[(\Lambda^{\alpha}+\Lambda^{\beta}+1)\phi\Big], \tag{A.3l}$$

$$J^{(\tau)}_{r_{\perp}\phi}(\boldsymbol{r}) = i\sum_{\alpha\gamma}\rho^{(\tau)}_{\alpha\gamma,-}\mathcal{F}^{4}_{\alpha\gamma}(r_{\perp},z)\cos\Big[(\Lambda^{\alpha}+\Lambda^{\beta}+1)\phi\Big], \tag{A.3m}$$

$$J^{(\tau)}_{r_{\perp}z}(\boldsymbol{r}) = \sum_{\alpha\gamma}\rho^{(\tau)}_{\alpha\gamma,+}\mathcal{F}^{4}_{\alpha\gamma}(r_{\perp},z)\sin\Big[(\Lambda^{\alpha}-\Lambda^{\beta})\phi\Big], \tag{A.3n}$$

$$J^{(\tau)}_{\phi r_{\perp}}(\boldsymbol{r}) = i\sum_{\alpha\gamma}\rho^{(\tau)}_{\alpha\gamma,-}\mathcal{F}^{7}_{\alpha\gamma}(r_{\perp},z)\cos\Big[(\Lambda^{\alpha}+\Lambda^{\beta}+1)\phi\Big], \tag{A.3o}$$

$$J^{(\tau)}_{\phi\phi}(\boldsymbol{r}) = -i\sum_{\alpha\gamma}\rho^{(\tau)}_{\alpha\gamma,-}\mathcal{F}^{7}_{\alpha\gamma}(r_{\perp},z)\sin\Big[(\Lambda^{\alpha}+\Lambda^{\beta}+1)\phi\Big], \tag{A.3p}$$

$$J^{(\tau)}_{\phi z}(\boldsymbol{r}) = \sum_{\alpha\gamma}\rho^{(\tau)}_{\alpha\gamma,+}\mathcal{F}^{5}_{\alpha\gamma}(r_{\perp},z)\cos\Big[(\Lambda^{\alpha}-\Lambda^{\beta})\phi\Big], \tag{A.3q}$$

$$J^{(\tau)}_{zr_{\perp}}(\boldsymbol{r}) = i\sum_{\alpha\gamma}\rho^{(\tau)}_{\alpha\gamma,-}\mathcal{F}^{6}_{\alpha\gamma}(r_{\perp},z)\sin\Big[(\Lambda^{\alpha}+\Lambda^{\beta}+1)\phi\Big], \tag{A.3r}$$

$$J^{(\tau)}_{z\phi}(\boldsymbol{r}) = i\sum_{\alpha\gamma}\rho^{(\tau)}_{\alpha\gamma,-}\mathcal{F}^{6}_{\alpha\gamma}(r_{\perp},z)\cos\Big[(\Lambda^{\alpha}+\Lambda^{\beta}+1)\phi\Big], \tag{A.3s}$$

$$J^{(\tau)}_{zz}(\boldsymbol{r}) = \sum_{\alpha\gamma}\rho^{(\tau)}_{\alpha\gamma,+}\mathcal{F}^{6}_{\alpha\gamma}(r_{\perp},z)\sin\Big[(\Lambda^{\alpha}-\Lambda^{\beta})\phi\Big]. \tag{A.3t}$$

Here, we have introduced a shorthand notation for density matrices

$$\rho^{(\tau)}_{\alpha\gamma,+} = \frac{1}{2\pi}\Big(\rho^{(\tau)++}_{\alpha\gamma}+\rho^{(\tau)--}_{\alpha\gamma}\Big), \tag{A.4a}$$

$$\rho^{(\tau)}_{\alpha\gamma,-} = \frac{1}{2\pi}\Big(\rho^{(\tau)++}_{\alpha\gamma}-\rho^{(\tau)--}_{\alpha\gamma}\Big), \tag{A.4b}$$

as well as for the coordinate-dependent factors

$$\mathcal{F}^{1}_{\alpha\gamma}(r_{\perp},z) = \psi_{n^{\alpha}_{z}}(z)\psi^{|\Lambda^{\alpha}|}_{n^{\alpha}_{\perp}}(r_{\perp})\psi_{n^{\beta}_{z}}(z)\psi^{|\Lambda^{\beta}|}_{n^{\beta}_{\perp}}(r_{\perp}), \tag{A.5a}$$

$$\mathcal{F}^{2}_{\alpha\gamma}(r_{\perp},z) = \psi_{n^{\alpha}_{z}}(z)\Big(\partial_{r_{\perp}}\psi^{|\Lambda^{\alpha}|}_{n^{\alpha}_{\perp}}(r_{\perp})\Big)\psi_{n^{\beta}_{z}}(z)\Big(\partial_{r_{\perp}}\psi^{|\Lambda^{\beta}|}_{n^{\beta}_{\perp}}(r_{\perp})\Big) + \frac{\Lambda^{\alpha}\Lambda^{\beta}}{r^{2}_{\perp}}\mathcal{F}^{1}_{\alpha\gamma}(r_{\perp},z) + \Big(\partial_{z}\psi_{n^{\alpha}_{z}}(z)\Big)\psi^{|\Lambda^{\alpha}|}_{n^{\alpha}_{\perp}}(r_{\perp})\Big(\partial_{z}\psi_{n^{\beta}_{z}}(z)\Big)\psi^{|\Lambda^{\beta}|}_{n^{\beta}_{\perp}}(r_{\perp}), \tag{A.5b}$$

$$\mathcal{F}^3_{\alpha\gamma}(r_\perp,z) = \psi_{n_z^\alpha}(z)\Big(\partial_{r_\perp}\psi^{|\Lambda^\alpha|}_{n_\perp^\alpha}(r_\perp)\Big)\psi_{n_z^\beta}(z)\Big(\partial_{r_\perp}\psi^{|\Lambda^\beta|}_{n_\perp^\beta}(r_\perp)\Big) - \frac{\Lambda^\alpha\Lambda^\beta}{r_\perp^2}\psi_{n_z^\alpha}(z)\psi^{|\Lambda^\alpha|}_{n_\perp^\alpha}(r_\perp)\psi_{n_z^\beta}(z)\psi^{|\Lambda^\beta|}_{n_\perp^\beta}(r_\perp) + \Big(\partial_z\psi_{n_z^\alpha}(z)\Big)\psi^{|\Lambda^\alpha|}_{n_\perp^\alpha}(r_\perp)\Big(\partial_z\psi_{n_z^\beta}(z)\Big)\psi^{|\Lambda^\beta|}_{n_\perp^\beta}(r_\perp), \tag{A.5c}$$

$$\mathcal{F}^4_{\alpha\gamma}(r_\perp,z) = \psi_{n_z^\alpha}(z)\Big(\partial_{r_\perp}\psi^{|\Lambda^\alpha|}_{n_\perp^\alpha}(r_\perp)\Big)\psi_{n_z^\beta}(z)\psi^{|\Lambda^\beta|}_{n_\perp^\beta}(r_\perp) - \psi_{n_z^\alpha}(z)\psi^{|\Lambda^\alpha|}_{n_\perp^\alpha}(r_\perp)\psi_{n_z^\beta}(z)\Big(\partial_{r_\perp}\psi^{|\Lambda^\beta|}_{n_\perp^\beta}(r_\perp)\Big), \tag{A.5d}$$

$$\mathcal{F}^5_{\alpha\gamma}(r_\perp,z) = \frac{(\Lambda^\alpha+\Lambda^\beta)}{r_\perp}\mathcal{F}^1_{\alpha\gamma}(r_\perp,z), \tag{A.5e}$$

$$\mathcal{F}^6_{\alpha\gamma}(r_\perp,z) = \Big(\partial_z\psi_{n_z^\alpha}(z)\Big)\psi^{|\Lambda^\alpha|}_{n_\perp^\alpha}(r_\perp)\psi_{n_z^\beta}(z)\psi^{|\Lambda^\beta|}_{n_\perp^\beta}(r_\perp) - \psi_{n_z^\alpha}(z)\psi^{|\Lambda^\alpha|}_{n_\perp^\alpha}(r_\perp)\Big(\partial_z\psi_{n_z^\beta}(z)\Big)\psi^{|\Lambda^\beta|}_{n_\perp^\beta}(r_\perp), \tag{A.5f}$$

$$\mathcal{F}^7_{\alpha\gamma}(r_\perp,z) = \frac{(\Lambda^\alpha-\Lambda^\beta)}{r_\perp}\mathcal{F}^1_{\alpha\gamma}(r_\perp,z). \tag{A.5g}$$

Furthermore, the local pairing densities read

$$\tilde\rho^{(\tau)}(\boldsymbol{r}) = \sum_{\alpha\gamma}\kappa^{(\tau)}_{\alpha\gamma,-}\mathcal{F}^1_{\alpha\gamma}(r_\perp,z)\cos\Big[(\Lambda^\alpha-\Lambda^\beta)\phi\Big], \tag{A.6a}$$

$$\tilde\rho^{*(\tau)}(\boldsymbol{r}) = \sum_{\alpha\gamma}\kappa^{*(\tau)}_{\alpha\gamma,-}\mathcal{F}^1_{\alpha\gamma}(r_\perp,z)\cos\Big[(\Lambda^\alpha-\Lambda^\beta)\phi\Big], \tag{A.6b}$$

with an equivalent shorthand notation

$$\kappa^{(\tau)}_{\alpha\gamma,-} = \frac{1}{2\pi}\Big(\kappa^{(\tau)+-}_{\alpha\gamma} - \kappa^{(\tau)-+}_{\alpha\gamma}\Big), \tag{A.7a}$$

$$\kappa^{*(\tau)}_{\alpha\gamma,-} = \frac{1}{2\pi}\Big(\kappa^{*(\tau)+-}_{\alpha\gamma} - \kappa^{*(\tau)-+}_{\alpha\gamma}\Big). \tag{A.7b}$$

Appendix B. Coupling constants of the Skyrme EDF

The time-even and time-odd contributions to the Skyrme EDF [cf. Eqs. (54) and (55), respectively] contain a total of twenty coupling constants in the isoscalar ($t=0$) and the isovector ($t=1$) channel. Four of these constants are density-dependent and can further be decomposed as

$$C^{\rho\rho}_{\boldsymbol{q},t}(\boldsymbol{r};\boldsymbol{x}) = C^{\rho\rho}_{t,0} + C^{\rho\rho}_{t,D}\rho^\alpha_{\boldsymbol{q}}(\boldsymbol{r};\boldsymbol{x}), \tag{B.1a}$$

$$C^{ss}_{\boldsymbol{q},t}(\boldsymbol{r};\boldsymbol{x}) = C^{ss}_{t,0} + C^{ss}_{t,D}\rho^\alpha_{\boldsymbol{q}}(\boldsymbol{r};\boldsymbol{x}). \tag{B.1b}$$

Here, the real number α can be considered as a parameter of an EDF. The remaining twenty four density-independent coupling constants can then be expressed in terms of the (t,x) parameters of the Skyrme EDF. In the time-even channel, the coupling constants read

$$C^{\rho\rho}_{0,0} = +\frac{3}{8}t_0, \tag{B.2a}$$

$$C^{\rho\rho}_{0,D} = +\frac{1}{16}t_3, \tag{B.2b}$$

$$C^{\rho\rho}_{1,0} = -\frac{1}{4}t_0\Big(\frac{1}{2}+x_0\Big), \tag{B.2c}$$

$$C^{\rho\rho}_{1,D} = -\frac{1}{24}t_3\Big(\frac{1}{2}+x_3\Big), \tag{B.2d}$$

$$C^{\rho\Delta\rho}_{0} = -\frac{9}{64}t_1 + \frac{1}{16}t_2\Big(\frac{5}{4}+x_2\Big), \tag{B.2e}$$

$$C^{\rho\Delta\rho}_{1} = +\frac{3}{32}t_1\Big(\frac{1}{2}+x_1\Big) + \frac{1}{32}t_2\Big(\frac{1}{2}+x_2\Big), \tag{B.2f}$$

$$C^{\rho\tau}_{0} = +\frac{3}{16}t_1 + \frac{1}{4}t_2\Big(\frac{5}{4}+x_2\Big), \tag{B.2g}$$

$$C^{\rho\tau}_{1} = -\frac{1}{8}t_1\Big(\frac{1}{2}+x_1\Big) + \frac{1}{8}t_2\Big(\frac{1}{2}+x_2\Big), \tag{B.2h}$$

$$C^{\rho\nabla J}_{0} = -b_4 - \frac{1}{2}b'_4, \tag{B.2i}$$

$$C^{\rho\nabla J}_{1} = -\frac{1}{2}b'_4, \tag{B.2j}$$

$$C^{JJ}_{0} = +\frac{1}{8}t_1\Big(\frac{1}{2}-x_1\Big) - \frac{1}{8}t_2\Big(\frac{1}{2}+x_2\Big), \tag{B.2k}$$

$$C^{JJ}_{1} = -\frac{1}{16}\Big(t_2-t_1\Big), \tag{B.2l}$$

where b_4 and b'_4 are the parameters of the spin-orbit force and we took $t_e = t_o = 0$ for the tensor terms [1]. In the time-odd channel, the coupling constants read

$$C^{ss}_{0,0} = -\frac{1}{4}t_0\Big(\frac{1}{2}-x_0\Big), \tag{B.3a}$$

$$C^{ss}_{0,D} = -\frac{1}{24}t_3\Big(\frac{1}{2}-x_3\Big), \tag{B.3b}$$

$$C^{ss}_{1,0} = -\frac{1}{8}t_0, \tag{B.3c}$$

$$C^{ss}_{1,D} = -\frac{1}{48}t_3, \tag{B.3d}$$

$$C^{s\Delta s}_{0} = +\frac{3}{32}t_1(\frac{1}{2}-x_1\Big) + \frac{1}{32}t_2\Big(\frac{1}{2}+x_2\Big), \tag{B.3e}$$

$$C^{s\Delta s}_{1} = +\frac{3}{64}t_1 + \frac{1}{64}t_2, \tag{B.3f}$$

$$C^{sj}_{0} = -C^{\rho\tau}_{0}, \tag{B.3g}$$

$$C^{sj}_{1} = -C^{\rho\tau}_{1}, \tag{B.3h}$$

$$C^{s\nabla j}_{0} = +C^{\rho\nabla J}_{0}, \tag{B.3i}$$

$$C^{s\nabla j}_{1} = +C^{\rho\nabla J}_{1}, \tag{B.3j}$$

$$C^{sT}_{0} = -C^{JJ}_{0}, \tag{B.3k}$$

$$C^{sT}_{1} = -C^{JJ}_{1}. \tag{B.3l}$$

Note that relations (B.3g) - (B.3l) are imposed by the local gauge invariance of an EDF [1].

References

[1] N. Schunck, Energy Density Functional Methods for Atomic Nuclei, IOP Expanding Physics, IOP Publishing, Bristol, UK, 2019.
[2] M. Bender, P.-H. Heenen, P.-G. Reinhard, Rev. Mod. Phys. 75 (1) (2003) 121.
[3] T. Nikšić, D. Vretenar, P. Ring, Prog. Part. Nucl. Phys. 66 (3) (2011) 519.
[4] L.M. Robledo, T.R. Rodríguez, R.R. Rodríguez-Guzmán, J. Phys. G, Nucl. Part. Phys. 46 (1) (2019) 013001.
[5] R.N. Perez, N. Schunck, R.-D. Lasseri, C. Zhang, J. Sarich, Comput. Phys. Commun. 220 (2017) 363.
[6] N. Schunck, J. Dobaczewski, W. Satuła, P. Bączyk, J. Dudek, Y. Gao, M. Konieczka, K. Sato, Y. Shi, X.B. Wang, T.R. Werner, Comput. Phys. Commun. 216 (2017) 145.
[7] W. Ryssens, V. Hellemans, M. Bender, P.-H. Heenen, Comput. Phys. Commun. 187 (2015) 175.
[8] T. Nikšić, N. Paar, D. Vretenar, P. Ring, Comput. Phys. Commun. 185 (6) (2014) 1808.
[9] B.G. Carlsson, J. Dobaczewski, J. Toivanen, P. Veselý, Comput. Phys. Commun. 181 (9) (2010) 1641.
[10] K. Bennaceur, J. Dobaczewski, Comput. Phys. Commun. 168 (2) (2005) 96.
[11] M.V. Stoitsov, J. Dobaczewski, W. Nazarewicz, P. Ring, Comput. Phys. Commun. 167 (1) (2005) 43.
[12] M. Stoitsov, N. Schunck, M. Kortelainen, N. Michel, H. Nam, E. Olsen, J. Sarich, S. Wild, Comput. Phys. Commun. 184 (6) (2013) 1592.
[13] J. Dobaczewski, P. Bączyk, P. Becker, M. Bender, K. Bennaceur, J. Bonnard, Y. Gao, A. Idini, M. Konieczka, M. Kortelainen, L. Próchniak, A.M. Romero, W. Satuła, Y. Shi, T.R. Werner, L.F. Yu, J. Phys. G, Nucl. Part. Phys. 48 (10) (2021) 102001.
[14] J.A. Sheikh, J. Dobaczewski, P. Ring, L.M. Robledo, C. Yannouleas, J. Phys. G, Nucl. Part. Phys. 48 (12) (2021) 123001.

[15] B. Bally, M. Bender, Phys. Rev. C 103 (2) (2021) 024315.
[16] D. Varshalovich, A. Moskalev, V. Khersonskii, Quantum Theory of Angular Momentum, World Scientific, Singapore, 1988.
[17] P. Ring, P. Schuck, The Nuclear Many-Body Problem, Texts and Monographs in Physics, Springer, 2004.
[18] V.N. Fomenko, J. Phys. A, Gen. Phys. 3 (1) (1970) 8.
[19] J.L. Egido, L.M. Robledo, Nucl. Phys. A 524 (1) (1991) 65.
[20] J. Dobaczewski, J. Dudek, S.G. Rohoziński, T.R. Werner, Phys. Rev. C 62 (1) (2000) 014310.
[21] J. Dobaczewski, J. Dudek, S.G. Rohoziński, T.R. Werner, Phys. Rev. C 62 (1) (2000) 014311.
[22] J.L. Egido, Phys. Scr. 91 (7) (2016) 073003.
[23] B. Avez, M. Bender, Phys. Rev. C 85 (3) (2012) 034325.
[24] A. Valor, P.H. Heenen, P. Bonche, Nucl. Phys. A 671 (1) (2000) 145.
[25] D. Baye, P.-H. Heenen, Phys. Rev. C 29 (3) (1984) 1056.
[26] L.M. Robledo, Phys. Rev. C 50 (6) (1994) 2874.
[27] R. Balian, E. Brezin, Nuovo Cimento B 64 (1) (1969) 37.
[28] K. Hara, S. Iwasaki, Nucl. Phys. A 332 (1) (1979) 61.
[29] P. Marević, N. Schunck, Phys. Rev. Lett. 125 (10) (2020) 102504.
[30] P. Marević, N. Schunck, J. Randrup, R. Vogt, Phys. Rev. C 104 (2) (2021) L021601.
[31] N. Onishi, S. Yoshida, Nucl. Phys. 80 (2) (1966) 367.
[32] R.G. Nazmitdinov, L.M. Robledo, P. Ring, J.L. Egido, Nucl. Phys. A 596 (1) (1996) 53.
[33] S.G. Rohoziński, J. Dobaczewski, W. Nazarewicz, Phys. Rev. C 81 (1) (2010) 014313.
[34] Y.M. Engel, D.M. Brink, K. Goeke, S.J. Krieger, D. Vautherin, Nucl. Phys. A 249 (2) (1975) 215.
[35] S. Perez-Martin, L. Robledo, Phys. Rev. C 78 (1) (2008) 014304, https://doi.org/10.1103/PhysRevC.78.014304.
[36] L.M. Robledo, Int. J. Mod. Phys. E 16 (02) (2007) 337–351.
[37] L.M. Robledo, J. Phys. G, Nucl. Part. Phys. 37 (6) (2010) 064020.
[38] A. Bulgac, M.M. Forbes, S. Jin, R.N. Perez, N. Schunck, Phys. Rev. C 97 (4) (2018) 044313.
[39] J. Dobaczewski, W. Nazarewicz, M.V. Stoitsov, in: The Nuclear Many-Body Problem 2001, in: Nato Science Series, vol. II, Springer, Netherlands, 2002, p. 181.
[40] A. Bulgac, Phys. Rev. C 65 (5) (2002) 051305(R).
[41] M. Girod, B. Grammaticos, Phys. Rev. C 27 (5) (1983) 2317.
[42] J. Dobaczewski, W. Satuła, B.G. Carlsson, J. Engel, P. Olbratowski, P. Powałowski, M. Sadziak, J. Sarich, N. Schunck, A. Staszczak, M. Stoitsov, M. Zalewski, H. Zduńczuk, Comput. Phys. Commun. 180 (11) (2009) 2361.
[43] J. Dobaczewski, W. Nazarewicz, T.R. Werner, J.F. Berger, C.R. Chinn, J. Dechargé, Phys. Rev. C 53 (6) (1996) 2809, https://doi.org/10.1103/PhysRevC.53.2809.
[44] M. Beiner, H. Flocard, N. Van Giai, P. Quentin, Nucl. Phys. A 238 (1) (1975) 29.
[45] E. Chabanat, P. Bonche, P. Haensel, J. Meyer, R. Schaeffer, Nucl. Phys. A 635 (1) (1998) 231.
[46] P.-G. Reinhard, D.J. Dean, W. Nazarewicz, J. Dobaczewski, J.A. Maruhn, M.R. Strayer, Phys. Rev. C 60 (1) (1999) 014316.
[47] A. Valor, J.L. Egido, L.M. Robledo, Phys. Lett. B 392 (3) (1997) 249.
[48] N. Schunck, Acta Phys. Pol. B 44 (2013) 263.
[49] M. Anguiano, J.L. Egido, L.M. Robledo, Nucl. Phys. A 696 (3–4) (2001) 467.
[50] J. Dobaczewski, M.V. Stoitsov, W. Nazarewicz, P.-G. Reinhard, Phys. Rev. C 76 (5) (2007) 054315.
[51] T. Duguet, M. Bender, K. Bennaceur, D. Lacroix, T. Lesinski, Phys. Rev. C 79 (4) (2009) 044320.
[52] M. Bender, T. Duguet, D. Lacroix, Phys. Rev. C 79 (4) (2009) 044319.
[53] N. Schunck, J.L. Egido, Phys. Rev. C 77 (1) (2008) 011301(R).
[54] N. Schunck, J.L. Egido, Phys. Rev. C 78 (6) (2008) 064305.
[55] E.M. Ney, J. Engel, T. Li, N. Schunck, Phys. Rev. C 102 (3) (2020) 034326.